Axon-specific microtubule regulation drives asymmetric regeneration of sensory neuron axons

Ana C. Costa [1,2], Blanca R. Murillo[1], Rita Bessa[1], Ricardo Ribeiro[1], Tiago Ferreira da Silva[3], Patrícia Porfírio-Rodrigues[4], Gabriel G. Martins[4], Pedro Brites[3], Matthias Kneussel[5], Thomas Misgeld[6], Monika S. Brill[6], Monica M. Sousa[1]*

[1] Nerve Regeneration Group, Instituto de Biologia Molecular e Celular (IBMC), Instituto de Investigação e Inovação em Saúde (i3S), University of Porto, Porto, Portugal

[2] Graduate Program in Molecular and Cell Biology, Instituto de Ciências Biomédicas Abel Salazar, University of Porto, Porto, Portugal

[3] Neurolipid Biology Group, Instituto de Biologia Molecular e Celular (IBMC), Instituto de Investigação e Inovação em Saúde (i3S), University of Porto, Porto, Portugal

[4] Advanced Imaging Unit, Instituto Gulbenkian de Ciência, Lisboa, Portugal

[5] Institute of Molecular Neurogenetics, Center for Molecular Neurobiology Hamburg, ZMNH, University Medical Centre Hamburg-Eppendorf, Hamburg, Germany

[6]Institute of Neuronal Cell Biology, Technical University of Munich, Munich, Germany; Munich Cluster for Systems Neurology (SyNergy), Munich, Germany

* Correspondence to Monica M Sousa: msousa@i3s.up.pt

Impact statement

Sensory neurons have a stem axon that bifurcates originating two axons with different properties. This work shows that DRG axons have a specific protein signature underlying microtubule and regeneration asymmetries. It also provides an *in vitro* system replicating DRG biology.

Abstract

Sensory dorsal root ganglion (DRG) neurons have a unique pseudo-unipolar morphology in which a stem axon bifurcates into a peripheral and a central axon, with different regenerative abilities. Whereas peripheral DRG axons regenerate, central axons are unable to regrow. Central axon regeneration can however be elicited by a prior conditioning lesion to the peripheral axon. How DRG axon asymmetry is established, remains unknown. Here we developed a rodent *in vitro* system replicating DRG pseudo-unipolarization and asymmetric axon regeneration. Using this model, we observed that from early development, central DRG axons have a higher density of growing microtubules. This asymmetry was also present *in vivo* and was abolished by a conditioning lesion that decreased microtubule polymerization of central DRG axons. An axon-specific microtubule-associated protein (MAP) signature, including the severases spastin and katanin and the microtubule regulators CRMP5 and tau, was found and shown to adapt upon conditioning lesion. Supporting its significance, interfering with the DRG MAP signature either *in vitro* or *in vivo*, readily abolished central-peripheral asymmetries in microtubule dynamics and regenerative ability. In summary, our data

unveil that axon-specific microtubule regulation drives asymmetric regeneration of sensory neuron axons.

Introduction

To execute their functions, neurons evolved a high degree of polarization (Banker, 2018). Sensory dorsal root ganglion (DRG) neurons show a unique pseudo-unipolar morphology in which a single stem axon bifurcates into a peripheral and a central axon, each with distinct functions and properties (Nascimento et al., 2018). The peripheral DRG axon is the site of action potential generation that is transmitted to the central axon, which synapses with second-order neurons. While the different environments in which the two DRG axons lie certainly play an important role in their distinctive features, axon-intrinsic properties have emerged. In this respect, peripheral DRG axons show larger diameters (Suh et al., 1984), higher axonal transport rates (Komiya and Kurokawa, 1978, Wujek and Lasek, 1983), and increased regenerative capacity (Komiya, 1981, Wujek and Lasek, 1983) when compared to central ones (reviewed in (Nascimento et al., 2018)).

Given the different competence of DRG axons to mount a regenerative response, DRG neurons have been widely used to study the regulation of axon regeneration. Interestingly, while DRG peripheral axons regrow following injury *in vivo*, the central axon only regenerates if a priming conditioning lesion to the peripheral axon is made (Neumann and Woolf, 1999, Richardson and Verge, 1987). This conditioning peripheral lesion induces molecular changes in DRG neurons enabling their central axons to acquire growth competence, even in an inhibitory environment (Hoffman, 2010, Mar et

al., 2014a). We have previously shown that injury to the DRG peripheral axon induces a global increase in axonal transport that extends to the central axon, supporting axon regeneration (Mar et al., 2014b). Since axonal transport relies on microtubule-based motors, microtubule organization in the DRG axons may determine their biological asymmetry. However, in contrast to multipolar neurons where microtubule polarity governs asymmetric distribution of cargoes (Tas et al., 2017), the mechanisms underlying differential axonal transport rates in DRG neurons are not understood. An important setback in studying DRG neurons is that while different structural aspects of their two axons may have important implications in their function, most of the studies are restricted to the use of *in vitro* systems in which these neurons fail to recapitulate their pseudo-unipolar morphology (Nascimento et al., 2018).

Here we established an *in vitro* model replicating DRG pseudo-unipolarization and asymmetric axon development that is an important tool to understand the biology of sensory neurons and the mechanisms underlying optimal axon (re)growth. Combining this *in vitro* model with *in vivo* studies, we show that axon-specific regulation of microtubule polymerization underlies regeneration asymmetry of sensory neuron axons.

Results

DRG neurons *in vitro* undergo pseudo-unipolarization, replicating *in vivo* asymmetries and regenerative capacity

To investigate the cellular and molecular mechanisms underlying the physiological asymmetries and regenerative capacity of DRG neurons, it is crucial to develop a primary cell culture system that promotes physiological cellular behavior. DRG neurons from developing or adult rodents cultured *in vitro* often fail to fully mimic their *in vivo* cell biology, typically producing multiple, highly ramified neurites (Nascimento et al., 2018). Ideally, DRG neuron cultures should replicate the morphogenic process of pseudo-unipolarization while preserving the peripheral-central axonal asymmetries (Nascimento et al., 2022). In this respect, we developed an *in vitro* system where, in the presence of DRG glial cells, pseudo-unipolarization occurs. In this system, during the early phases of development, DRG neurons exhibit a spindle or eccentric-shaped bipolar morphology (Figure 1A, stage I), and as they mature the two axons move closer, adopting a bell-shaped bipolar morphology (Figure 1A, stage II), that later converts into a pseudo-unipolar morphology (Figure 1A, stage III). At DIV21, we observed 4±1% multipolar (with more than two neurites), 35±8 % bipolar, 17±5 % bell-shaped, and 43±3 % pseudo-unipolar DRG neurons (Figure 1B). When we segmented pseudo-unipolar DRG neurons, the stem axon and the bifurcating axons were clearly observed (Figure 1C and Figure 1 - video 1). While DRG neurons undergo pseudo-unipolarization (Figure 1D and Figure 1 - video 2), a reduction in diameter (Figure 1D-E) coupled with an increased length of the stem axon (Figure 1D and 1F) occurs, mirroring *in vivo* development (Matsuda et al., 2000). To further understand stem axon formation, we tracked the

displacement of the DRG T-junction (Figure 1D, black arrowhead) and of the top of the cell body (Figure 1D, green arrowhead) in relation to the initial position of the T-junction (Figure 1D, red dot). After establishing the DRG T-junction, the cell body is displaced significantly to the opposite direction (Figure 1D- green arrowhead; and 1G), while the position of the base of the stem axon remains relatively stable (Figure 1D, black arrowhead; and 1G). This supports that cell body bulging participates in stem axon formation, as previously suggested (Matsuda et al., 2000). Interestingly, at early days *in vitro* (DIV 7-14), pseudo-unipolar DRG could be reverted to a bell-shaped bipolar morphology, while at later DIVs (DIV 14-21), this transition was never observed (Figure 1 - video 2). *In vivo* studies have shown that peripheral and central DRG axons differ in diameter, with peripheral axons being larger (Suh et al., 1984). When measuring the two bifurcating axons 3-5 µm away from the DRG T-junction, we observed that pseudo-unipolar DRG neurons exhibit two axons with distinct diameters: a thin, central-like branch and a thicker, peripheral-like branch (Figure 1H-I). This axonal diameter asymmetry is established early in DRG development, as bipolar neurons already displayed axons of different diameters (Figure 1H).

To further support the relevance of our *in vitro* system, we explored whether it replicates the observed *in vivo* asymmetry in regenerative capacity. For that, either the large peripheral-like (Figure 2A and Figure 2 - video 1) or the thin central-like axon (Figure 2B and Figure 2 - video 1) were injured by laser axotomy and their regenerative response was followed. While the length of retraction following injury was the same for both DRG axons (Figure 2C), the duration of retraction was higher in central-like axons (Figure 2D), suggesting that these require more time to assemble a regenerative

response (Koseki et al., 2017). Moreover, whereas over 50% of the injured peripheral-like axons were able to regenerate with an average length of 33.4 µm, only approximately 10% of injured central ones showed the same ability, with a 3.8-fold decreased length (8.7 µm), (Figure 2E-F).

In summary, we established an *in vitro* system that mirrors the physiological developmental stages of DRG neurons *in vivo*, recapitulating their regenerative asymmetries. This model is a valuable tool for studying the unique biology of DRG neurons as well as for investigating the mechanisms driving axon regeneration.

DRG axons exhibit asymmetric microtubule polymerization, which is downregulated by a conditioning lesion

Early studies demonstrated that axonal transport is asymmetrically regulated in DRG axons, as peripheral axons exhibit higher transport rates (reviewed in (Nascimento et al., 2018). Aligning with *in vivo* data, in our *in vitro* model, peripheral-like axons had a higher flux of anterogradely moving mitochondria than central-like axons (Figure 3A and 3B and Figure 3- video 1), further supporting the relevance of this system. Given the importance of microtubules in axonal transport (Nirschl et al., 2017), we next investigated how microtubule dynamics is regulated in peripheral and central-like axons *in vitro*. Using the microtubule plus-tip end-binding protein 3 (EB3) to track growing microtubules plus-tips (Stepanova et al., 2003), we observed that while both DRG axons had microtubule plus-end-out polarity (Figure 3 – video 2), the central-like axon had a greater density of growing microtubules (Figure 3C-D), and a slower microtubule growth rate (Figure 3E). Notably, microtubule polymerization asymmetry was

established early in DRG development, as it was already present in bipolar DRG neurons (Figure 3C).

The observation of microtubule asymmetries in DRG axons *in vitro* led us to investigate whether similar asymmetries exist *in vivo*. For that, we used Thy1-EB3-eGFP transgenic mice (Kleele et al., 2014), which express EB3-eGFP in neurons. DRG explants, including both the DRG peripheral nerve (containing peripheral axons) and the dorsal root (containing central axons) connected to the DRG ganglia (containing DRG cell bodies) were collected and immediately imaged for up to 1 hour, proximal to the DRG ganglia (Figure 3F, dashed box). In both central and peripheral DRG axons, most microtubules moved with plus-end-out polarity (94% and 95% respectively) (Figure 3G and Figure 3 – video 3), as observed *in vitro* (Figure 3 – video 2). Also replicating our *in vitro* observations (Figure 3C), central DRG axons exhibited an increased density of growing microtubules (Figure 3H, naive), which was unrelated to differences in total microtubule density (Figure 3I-J). Interestingly, and again replicating *in vitro* findings (Figure 3E), although having a higher density of growing microtubules, these grew at slower growth rates in central DRG axons (Figure 3K, naive). In summary, our findings indicate that although both axons originate from the same stem axon and share the same polarity, each DRG axon has distinct regulatory mechanisms governing its microtubule dynamics.

We next explored if this physiological asymmetry in microtubule polymerization is regulated after a conditioning lesion, where a global increase in axonal transport sustains central axon regeneration (Mar et al., 2014b). The shaft of peripheral and central DRG axons was imaged on explants 1.0-1.5 centimeters from the lesion site,

one-week post-lesion (Figure 3L, dashed box). Uninjured DRG explants were used as controls. A conditioning lesion decreased the density of growing microtubules not only in the peripheral DRG axon but this effect extended to the central DRG axon (Figure 3H, conditioning lesion), abolishing central-peripheral asymmetry. This was unrelated to differences in total microtubule density, as determined by electron microscopy (Figure 3M). In addition to decreasing the density of growing microtubules, a conditioning lesion increased the velocity of microtubule polymerization both in peripheral and central DRG axons (Figure 3K, conditioning lesion). Taken together, our findings show that injury to the peripheral DRG axon regulates microtubule dynamics in the shaft of both DRG axons, decreasing the density of growing microtubule plus-tips in central axons.

DRG axons have a distinctive MAP signature that adapts upon conditioning lesion

To understand the mechanisms underlying asymmetry in microtubule dynamics in DRG axons, and its modulation by conditioning lesion, we analyzed tubulin post-translational modifications (PTMs) (Janke and Magiera, 2020) and microtubule-associated protein (MAPs) (Bodakuntla et al., 2019) levels in DRG explants. We specifically selected the microtubule severing enzymes spastin and katanin as these enhance the formation of new microtubule plus-ends (Kuo and Howard, 2021). Whereas tubulin PTM levels were identical in both DRG peripheral nerve and dorsal root (Figure 4 – figure supplement 1), the microtubule severases spastin and katanin were markedly increased in DRG central axons (Figure 4B-C and 4F). In the case of spastin, the lack of specific antibodies for immunofluorescence precluded tissue analysis. Recently, the microtubule regulators

CRMP5 (Ji et al., 2018, Jin et al., 2022) and tau (Kadavath et al., 2015, Panda et al., 1995, Siahaan et al., 2019, Tan et al., 2019) were shown to inhibit the action of spastin and katanin by blocking their access to the microtubule lattice. Interestingly, DRG peripheral axons had increased levels of both microtubule regulators (Figure 4D-E and 4G-H), which by restricting severase access to microtubules, may contribute to their decreased density of microtubule growing ends (Figure 3H, naive). Of note, CRMP5, similarly to CRMP2 (Fukata et al., 2002, Hou, 2020), may further support microtubule polymerization, enhancing microtubule growth rates in DRG peripheral axons (Figure 3K, naive). Hence, our data reveals that each DRG axon has a highly specific MAP signature that may support asymmetric microtubule polymerization.

Since microtubule dynamics adapts following conditioning lesion (Figure 3H and 3K), we analyzed whether it modulates the DRG MAP signature (Figure 4I). Interestingly, upon conditioning lesion, the uneven distribution of spastin, katanin, and CRMP5 in naive DRG (Figure 4B-D) was lost (Figure 4J-L). Importantly, the persistent asymmetry in tau distribution (Figure 4E and 4M) suggests that this MAP might be specifically related to the establishment of the structural differences between peripheral and central DRG axons.

The distinct MAP signatures of both DRG axons may arise from asymmetric axonal transport of mRNAs or proteins and/or differential local protein translation. However, as the density of spastin and CRMP5 transcripts in DRG axons was similar (Figure 4 – figure supplement 2A-C), differential mRNA transport and local translation probably do not account for asymmetric distribution of these proteins. An alternative mechanism to establish asymmetry of DRG axons may rely on distinct microtubule

streams entering peripheral and central axons. This is supported not only by early structural data (Ha, 1970), but also by our current *in vitro* model showing that microtubule asymmetry in DRG axons is established early in development. If these distinct streams exhibit different properties, they could guide specific cargoes to either central or peripheral axons. To investigate the arrangement of microtubules at the DRG T-junction, we analyzed *in vitro* DRG pseudo-unipolar neurons expressing EB3-GFP (Figure 4 – figure supplement 2D) that allowed to assess whether microtubule polymerization is arrested (Figure 4 – figure supplement 2E) or if a continuum of polymerization exists between the stem axon after the DRG bifurcation (Figure 4 – figure supplement 2F). In peripheral-like axons, similar numbers of EB3 comets stopped or crossed past the bifurcation point (Figure 4 – figure supplement 2G). Conversely, in DRG central-like axons, a ratio of 3:1 microtubules polymerized beyond the bifurcation point, supporting a higher microtubule continuum from the stem to the central-like axon (Figure 4 – figure supplement 2G). As specific tubulin PTMs can favor the binding of particular motors (Iwanski and Kapitein, 2023), we investigated whether microtubules entering each DRG neuron axon at the DRG T-junction had different PTMs. While the levels of polyglutamylated and acetylated tubulin (Figure 4 – figure supplement 2H-K) were the same in the two DRG axon compartments, Δ2 tubulin was the single PTM that was unevenly distributed, being increased in central-like axons (Figure 4 – figure supplement 2L-M). Overall, it is possible that at the DRG T-junction, distinct PTMs and microtubule polymerization patterns may serve as mechanisms for selectively directing cargoes into specific DRG axons.

Spastin deficiency is sufficient to abolish the asymmetry of DRG axons

To demonstrate the importance of the specific MAP signature of DRG axons, we investigated whether the absence of one of the signature proteins, spastin, was sufficient to affect DRG molecular asymmetries. *In vitro,* in wild-type and spastin knockout (Brill et al., 2016) DRG neurons*,* the lack of spastin abolished axonal microtubule polymerization asymmetry (Figure 5A-B). We then crossed spastin knockout mice with the Thy1-EB3-eGFP mouse line to test if this effect was also seen *in vivo*. Live imaging of DRG explants from spastin knockout X Thy1-EB3-eGFP mice showed that the absence of this enzyme was sufficient to abolish the asymmetry of microtubule polymerization in DRG axons, both in terms of EB3 comet density (Figure 5C-D) and velocity (Figure 5E-F), while total microtubule density was preserved (Figure 5 – figure supplement 1A). Together, our results show that interfering with a single protein of the DRG MAP signature is sufficient to disrupt the axonal asymmetry of microtubule polymerization.

Since spastin deficiency disrupted microtubule polymerization asymmetry of DRG axons, we then analyzed if it was sufficient to disrupt the conditioning lesion effect *in vivo*. At the time point at which lesions were performed uninjured wild-type and spastin knockout animals had a similar density of dorsal column tract (Figure 5 – figure supplement 1B) and sciatic nerve axons (Figure 5 – figure supplement 1C-D), ruling out primary defects of these tracts. For conditioning lesion, mice of both genotypes were subjected to sciatic nerve transection one week prior to spinal cord dorsal hemisection (Figure 5G and 5I-J); wild-type animals with spinal cord injury alone were used as controls (Figure 5H). Regeneration was assessed six weeks post-spinal cord dorsal

hemisection. In wild-type mice, conditioning lesion led to a substantial increase in the number of cholera toxin-positive regenerating DRG central axons (Figure 5I and 5K). In contrast, in spastin knockout mice, the conditioning lesion effect severely reduced the number of central DRG axons being able to grow in the inhibitory environment of the lesion site (Figure 5J-K). As a generalized spastin knockout mouse was used, to further support a neuron-specific effect, adult wild-type and spastin knockout DRG neuron monocultures were grown on aggrecan to mimic the proteoglycan inhibitory environment formed upon spinal cord injury. Under these conditions, spastin knockout DRG neurons extended 3.3-fold less primary neurites than wild-type DRG neurons (Figure 5L-M), replicating our *in vivo* findings. This indicates that loss of spastin in DRG neurons impairs axon growth under inhibitory conditions. In summary, interfering with the DRG MAP signature disrupts the asymmetry in microtubule polymerization of DRG axons as well as their ability to mount the conditioning effect.

Discussion

DRG neurons are a striking example of polarity. An intriguing question concerning DRG biology is how peripheral and central axons linked to the same stem axon display different properties. One major setback in the field was the lack of an *in vitro* system recapitulating DRG development, pseudo-unipolarization and establishment of polarity. Here, we developed an *in vitro* model where DRG neurons pseudo-unipolarize and mirror *in vivo* asymmetries, comprising those found in axon diameter, regenerative capacity, axonal transport, and microtubule dynamics (Figure 6A). This model serves as a valuable resource to understand DRG neuron biology (including stem axon formation

and possible sorting at the DRG T-junction), mechanisms driving axon regeneration asymmetries, and DRG-related diseases. Regarding DRG stem axon formation, our findings support that it may be driven by cell body bulging rather than fusion of the two neurites, aligning with previous studies (Matsuda et al., 2000). Concerning potential asymmetries in protein transport and microtubule dynamics at the DRG T-junction, while investigating these *in vivo* is challenging due to the length of the stem axon and the difficulty of imaging the T-junction, they can now be effectively studied using our *in vitro* system. Future studies should further address neuron-intrinsic mechanisms driving pseudo-unipolarization (such as the role of cytoskeletal dynamics, and of Golgi and nuclear positioning), as well as the influence of extrinsic factors, namely the identify of specific DRG glial cells supporting pseudo-unipolarization. While the current model focuses on features shared across DRG subtypes, such as pseudo-unipolarization and the higher regenerative capacity of peripheral branches, whether it favors specific DRG subtypes should be further explored. *In vitro* models resourcing to DRG explants and the development of compartmentalized systems with peripheral and central targets could provide additional insights into pseudo-unipolarization, regenerative capacity, and target re-innervation. However, although previous compartmentalized DRG cultures have been reported (Giorgi et al., 2023, Vikman et al., 2001), these have not demonstrated pseudo-unipolarization.

We found that the asymmetric microtubule dynamics of peripheral and central DRG axons, that is observed both *in vitro* and *in vivo*, is supported by a distinct MAP signature that promotes a higher density of growing microtubules in central axons (Figure 6B). Despite scattered reports in the literature, markers of distinct DRG axons

remained unidentified (Garcia-Anoveros et al., 2001, Katano et al., 2006, Papasozomenos et al., 1985) and early studies suggested that similar proteins are transported to both DRG axons (Bisby, 1981, Perry and Wilson, 1981, Stone and Wilson, 1979). Our data shows however that the content of specific microtubule modulators including severases and the microtubule regulators CRMP5 and tau are axon-specific in DRG neurons. Other MAPs, such as MAP2, show however no differences between the two DRG axons. The mechanisms underlying this differential protein distribution remain unclear. One hypothesis is that mRNAs or proteins, are asymmetrically transported at the DRG T-junction. While our data show no significant differences in the density of *spastin* and *CRMP5* mRNA between both DRG axons, the possibility of asymmetric protein transport cannot be ruled out. Recently, a pre-axonal cargo filtering zone mediated by MAP2 was identified in DRG neurons (Gumy et al., 2017). Although this may partially establish two separate compartments – the cell body and axons – how cargo filtering takes place at the DRG T-junction remains unknown. In multipolar neurons, differential cargo sorting to dendrites or axons is achieved through the axon initial segment (AIS) (Song et al., 2009) and by the distinct microtubule polarity in axons and dendrites (Zheng et al., 2008). Similar mechanisms are however difficult to envisage in DRG neurons. Not only microtubules in both DRG axons are oriented plus-ends out, but also the AIS of DRG neurons is located in the stem axon proximal to the DRG cell body (Nascimento et al., 2022). An alternative mechanism to establish asymmetry of DRG axons may rely on distinct microtubule streams entering peripheral and central axons as supported by early structural data (Ha, 1970). In fact, our data suggest that there is a preferential continuous microtubule polymerization from the DRG

stem axon into the central-like axon that is accompanied by increased Δ2 tubulin levels. This differential microtubule organization may serve as a mechanism for cargo filtering between DRG axons. In chemotherapy-induced peripheral neuropathy, the accumulation of Δ2 tubulin in DRGs and peripheral nerves disrupts mitochondrial motility (Pero et al., 2021). Accordingly, at the DRG T-junction the anterograde transport of mitochondria is biased towards the DRG peripheral-like axon, where Δ2 tubulin levels are reduced. It is thus possible that Δ2 tubulin interferes with binding of molecular motors, contributing to establish a cargo filtering mechanism at the DRG T-junction. In the future, it would be valuable to investigate whether microtubules at the DRG T-junction intermix or segregate as separate pools as they extend from the cell body towards the bifurcation.

DRG neurons are a powerful model to study axon regeneration given the distinct regenerative capacity of their axons, and the fact that a peripheral conditioning lesion enables regeneration of central axons (Neumann and Woolf, 1999, Richardson and Verge, 1987). We previously demonstrated that a conditioning lesion elicits a global increase in axonal transport that extends to the central DRG axon, allowing rapid and sustained support of central axon regrowth (Mar et al., 2014b). Here we show that a conditioning lesion also induces alterations in the DRG microtubule cytoskeleton, decreasing the density of growing microtubules through an adaptive response of the MAP signature of DRG axons (Figure 6C). This decrease in microtubule dynamics extends away from the injury site, propagating to the distant axon shaft of both DRG branches. The study of changes in axonal microtubule dynamics has been mostly restricted to local effects in the growth cone. In this compartment, low doses of the

microtubule-stabilizing drug taxol reduce the percentage of retraction bulbs after central axon injury (Erturk et al., 2007, Hellal et al., 2011). Microtubule stabilization is also crucial to sustain efficient axonal transport, with taxol-stabilized microtubules enhancing kinesin binding (Dunn et al., 2008, Kapitein et al., 2010). Likewise, the reduction in growing microtubule density following a conditioning lesion may contribute to microtubule stabilization, supporting axonal transport and regeneration. Similarly to the growth cone where a delicate balance between microtubule stabilization and dynamics is necessary, a balanced regulation of microtubule dynamics in the axon shaft may also be required, as excessive stabilization may be detrimental (Gornstein and Schwarz, 2017, Pero et al., 2021).

Maintaining the MAP signature is crucial for preserving the physiology and regenerative capacity of DRG neurons. Our data strongly underscore the significance of this signature, showing that the loss of spastin disrupts microtubule asymmetry in DRG neurons and results in reduced central axon regeneration (Figure 6D). Examining the effects of depleting other MAPs, such as katanin and CRMP5, which lose their asymmetry following conditioning lesion, could offer additional valuable insights into their roles in maintaining DRG axon asymmetry and supporting axon regeneration. Notably, katanin shares similar severing mechanisms with spastin (Roll-Mecak and Vale, 2008, Zehr et al., 2017) and is partially regulated in a comparable manner. Both proteins undergo biphasic regulation through tubulin glutamylation (Lacroix et al., 2010, Szczesna et al., 2022, Valenstein and Roll-Mecak, 2016) and their severing activity is inhibited by tau condensates (Siahaan et al., 2019, Tan et al., 2019). Moreover, katanin plays a role in axon outgrowth (Ahmad et al., 1999, Chen et al., 2014), with RhoA

negatively modulating neurite outgrowth via regulation of spastin and katanin (Tan et al., 2020). Despite not being functionally redundant, it is possible that katanin deficiency may impact DRG microtubule asymmetry and regenerative capacity similarly to spastin. In summary, our data unveil that axon-specific microtubule regulation drives asymmetric regeneration of sensory neuron axons. We further provide a *bona fide* model of DRG pseudo-unipolarization and establishment of axonal asymmetry that will contribute to push forward our understanding of sensory neuron biology and of axon growth and regeneration.

Materials and Methods

Culture of pseudo-unipolar DRG neurons

DRG cultures from Wistar rats (embryonic day 16) and spastin knockout mice and wild-type littermates (embryonic day 13) were done as previously described (Nascimento et al., 2022). These developmental stages in rats and mice yield DRG neuron cultures with similar percentages of pseudo-unipolarization. Briefly, DRGs were isolated and mechanically dissociated, digested with trypsin 0.05 % EDTA (#25300062, Gibco) for 1 h at 37°C, centrifuged at 200 g, and mechanically dissociated with a 1000µl micropipette, in the final culture medium (Neurobasal medium supplemented with 2% B27 (#17504044, Gibco), 2 mM L-glutamine, 1% penicillin–streptomycin and 50 ng/ml of nerve growth factor (#N-100, Millipore)). Cells were then seeded either at 27,000 (for analyzes of microtubule polymerization), at 7,000 (for studies using laser ablation and stem axon formation), or at 3,000 (for immunocytochemistry) cells/well in glass-bottom 4-well chambered coverslips (#80427, Ibidi) (for live imaging) or in 24-well plates (for

immunocytochemistry), previously precoated with 20 µg/mL poly-L-lysine and 5 µg/mL laminin. Cultures were maintained at 37°C in a 5% CO_2 incubator and the medium was partially changed once a week for 21 days, a time point at which pseudo-unipolarization occurs in approximately 43±3 % of cultured DRG neurons. Pseudo-unipolar DRG neurons were identified based on the following criteria: the presence of a clearly discernible stem axon measuring at least 10 µm in length, with the proximal region of the bifurcating axons devoid of crossing neurites within a distance of 20–30 µm, ensuring an unobstructed area for analysis. Peripheral-like and central-like axons were distinguished by consistently measuring their diameters across all experiments.

Analysis of stem axon formation in DRG neuron cultures

To investigate the *in vitro* formation of the stem axon in DRG neuron development, we transduced these cells with an ultra-purified recombinant AAVPHP.S-CMV-eGFP (#VB010000-9394npt, VectorBuilder) virus at DIV 9 at a concentration of 1.12 x 10^{10} cfu/ 7000 cells. We live imaged the cells for 7 consecutive days from DIV 14-21. Approximately 30 bipolar and bell-shaped DRG neurons per well, exhibiting a low to moderate eGFP expression, were selected. Imaging was performed using a widefield inverted microscope, Nikon ECLIPSE Ti (Nikon, Japan), equipped with an Iris 9 sCMOS camera (Photometrics) and a CFI Plan Apochromat Lambda D 40X/0.95 DIC objective, and controlled through the NIS elements 5.4 software (Nikon, Japan). eGFP excitation was achieved using the Lumencor Spectra X Cyan 470/24 with LED % of 10, an exposure time of 200 ms, in combination with the following filters: excitation filter: FF01-387/485/559/649; dichroic: FF410/504/582/669-Di01; emission filter: FF01-

440/521/607/700. Images were acquired every hour. Gray levels were inverted for improved visualization. Due to the random nature of viral infection and the potential light-induced toxicity associated with the longitudinal imaging setup, only a subset of the 30 selected neurons underwent pseudo-unipolarization in each experiment. To quantify the initial and final diameter and length of the stem axon, the Fiji/ImageJ segmented line tool was employed. To quantify the displacement of the base of the stem axon and of the top of the DRG cell body, we used the initial position of the base of the DRG T-junction as a reference point. Using this reference point, we tracked the displacement of both the base of the stem axon and the top of the cell body using the MTrackJ plugin in ImageJ/Fiji software. For DRG segmentation, we acquired pseudo-unipolar eGFP-positive DRG neurons at DIV14 using an inverted Leica SP8 single-point scanning confocal microscope (Leica Microsystems, Germany) and Leica Application Suite X software (version 3.5.7.23225, RRID:SCR_013673). All images were scanned unidirectionally at 400 Hz using the galvanometer-based imaging mode, with a z-step size of 0.2 µm. The final image resolution was 0.12 µm/pixel. Pseudo-unipolar DRG neurons were selected for segmentation using Imaris software (version 10.1.1). The Imaris Surfaces tool was applied to extract a 3D object from the DRG neuron outer contour, using an intensity threshold to distinguish the cell from the background. We then used the Imaris Animation tool to create a video of the segmented DRG neuron.

Axotomy of cultured pseudo-unipolar DRG neurons

To study the regenerative capacity of pseudo-unipolar DRG neurons *in vitro*, we performed a laser axotomy of large and small-diameter axons. At DIV 15, rat DRG

neurons were transduced with an ultra-purified recombinant AAVPHP.S-CMV-eGFP (#VB010000-9394npt, VectorBuilder) virus at 1.12 x 10^{10} cfu/ 7000 cells. At DIV 21 neurons were live imaged using an inverted 3i Marianas Spinning Disk confocal system with an Yokogowa W1 scanhead + illumination Uniformizer, a Prime 95b sCMOS camera, mounted on a fully motorized Nikon Ti2-E microscope, and using a CFI Plan Apo VC 60XC 1.2 water/silicone immersion objective. The system was also equipped with a 3i Vector (galvo-based laser positioning unit) + 3i !Ablate unit with a 355nm pulsed laser. DRG neurons were first pre-screened to select target axons to injure (100-200 µm distally from the bifurcation point of the stem axon) and the areas to be imaged; six pseudo-unipolar DRG neurons were selected per experiment. eGFP was excited using a 488 nm laser line with a laser power of 7%. Laser ablation was performed on both large and small diameter axons using a 355 nm laser line that creates accurate and precise injuries to single axons while minimizing damage to nearby cells (Cengiz et al., 2012). We limited the injuries to a laser power of 50% and restricted them to three pulses per axon. Injuries were performed at 100–200 µm from the stem axon to minimize disruptions to intracellular homeostasis, which are more pronounced in lesions closer to the cell body and may lead to cell death (Cengiz et al., 2012). To ensure clear visualization of the regeneration process, neurons were selected when no crossing neurites from other cells were found within 100–200 µm of the stem axon. Imaging conditions and images were acquired using the Slidebook software (version 2022, RRID:SCR_014423) with a pinhole size of 50 µm and a final image resolution of 0.18 µm/pixel. All images were acquired every 4 minutes for 5 hours. Five independent experiments were performed to analyze axon retraction (length and duration) and axon

regeneration (regenerative length and frequency of regenerating versus non-regenerating axonal branches). Only axons that grew throughout the 300 frames (5h) were considered regenerating axons. Gray levels were inverted to facilitate visualization.

Live imaging of mitochondria transport in pseudo-unipolar DRG neuron cultures

DRG neurons from E16 Wistar rats were maintained in culture until DIV 21. Forty hours before live imaging, cells were transduced with a lentivirus expressing synapsin-Tom20-GFP (#BLV-569a, Charité NeuroCure, University of Berlin) at 7.07 x 10^5 cfu / 7.000 cells. Images were acquired using an inverted Leica SP8 single-point scanning confocal microscope (Leica Microsystems, Germany) and a Leica Application Suit X software (version 3.5.7.23225). All images were acquired every 2 seconds, for 63 frames, scanning unidirectionally at 400 Hz, using the galvanometer-based imaging mode, a line average of 3, and a digital zoom of 3x. Experiments were conducted at 37ºC and 5% CO_2. All images had a final resolution of 0.12 µm/pixel. Only pseudo-unipolar DRG neurons with low-to-moderate expression levels of Tom20-GFP were selected. The flux of anterogradely moving mitochondria in the DRG large and thin axons was determined as the number of mitochondria crossing a vertical line (placed in the middle of the axon) per minute. Five pseudo-unipolar DRG neurons were quantified in each experiment.

Live imaging of microtubule polymerization in pseudo-unipolar DRG neuron cultures

DRG neurons from E16 Wistar rats, and E13 spastin knockout mice were maintained in culture for 21 days *in vitro*. Forty hours before live imaging, cells were transduced with a lentivirus expressing CMV-EB3-GFP (from Franck Polleux) at 2.7 x 10^4 cfu / 27.000 cells. Images were acquired using an inverted Leica SP8 single-point scanning confocal microscope and a Leica Application Suit X software. All images were acquired every 2 seconds, for 46 frames, scanning unidirectionally at 400 Hz, using the galvanometer-based imaging mode, a line average of 4, and a digital zoom of 3.25x. Experiments were conducted at 37ºC and 5% CO_2. All images had a final resolution of 0.11 µm/pixel. Only bipolar and pseudo-unipolar DRG neurons with low-to-moderate expression levels of EB3-GFP were selected. The EB3-GFP comet velocity and density were quantified through kymographs using the Fiji/ImageJ KymoResliceWide plugin (https://github.com/ekatrukha/KymoResliceWide) or the KymoToolBox plugin (Zala et al., 2013). Gray levels were inverted to facilitate visualization. A segmented line was drawn over the DRG stem, large and thin axons, in the direction cell body-axon tip, and maximum intensity was extracted across the line width, when using the KymoResliceWide plugin. For EB3-GFP comets analyzed using the KymoResliceWide plugin, starting and end positions of the kymograph traces were defined using the Fiji/ImageJ Cell Counter plugin. The x-axis and y-axis coordinates of each trace were used to calculate the EB3-GFP comet velocity (distance, x-axis; time, y-axis). EB3-GFP comet density was calculated by dividing the total number of EB3-GFP comets counted within one kymograph by the area of the segmented line. For EB3-GFP comets analyzed using the KymoToolBox plugin, comet trajectories were manually identified using the segmented line tool. Approximately five to ten bipolar and pseudo-unipolar

DRG neurons were quantified in each experiment. The videos used to quantify EB3-GFP comet dynamics were used to quantify axon diameter in *in vitro* bipolar and pseudo-unipolar DRG neurons. For that, the diameter of the stem, large and thin axons was determined using the straight-line tool from Fiji/ImageJ to trace a perpendicular line connecting the two axon membrane borders. The videos of pseudo-unipolar DRG neurons where the stem, large, and thin axons were located on the same focal plane were used to quantify the total number of EB3-GFP comets that stop and cross the DRG T-junction. The number of EB3-comets that cross or stop at the DRG T-junction were traced using the composite panel obtained after analysis with the KymoToolBox plugin in a length of approximately 5 µm comprising the final part of the stem axon and the beginning of the large or thin axon.

Animals

Animal experiments followed EU Directive 2010/63/EU and national Decree-law number 113-2013, approved by the i3S Ethical Committee and Portuguese Veterinarian Board. Unless otherwise stated, C57BL/6 adult mice at 8-11 weeks of age were used. Thy1-EB3-eGFP mouse line was used to study microtubule polymerization (Kleele et al., 2014). Constitutive spastin knockout mice (Brill et al., 2016) and wild-type littermates were used and genotyped as detailed in (Brill et al., 2016). Mouse strains and Wistar rats were bred at the i3S animal facility, maintained with *ad libitum* access to water/food, and kept on a 12-hour light/dark cycle under controlled temperature and humidity. Animals of both genders were used in the experiments.

Animal surgeries

For sciatic nerve injury (peripheral injury), bilateral sciatic nerve transection was done in adult mice 2 mm proximal to the sciatic nerve trifurcation. Analgesia was provided to animals (3 mg buprenorphine/kg; administered twice a day). One week later, the mice were euthanized, and lumbar DRG L3, L4 and L5 explants were isolated. For live imaging experiments, both the dorsal root (containing central DRG axons) and the peripheral nerve (containing peripheral DRG axons) were imaged attached to the DRG ganglia, while for western blots, immunohistochemistry, electron microscopy, and RNAscope, the dorsal root, and the peripheral nerve were separated from the ganglia.

For central lesions, wild-type and *spastin* knockout mice underwent spinal cord dorsal hemisection at the T8 level using a micro-feather ophthalmic scalpel (#72045-45, Delta Microscopes). For conditioning lesions, a bilateral complete sciatic nerve transection was performed first, followed a week later by spinal cord dorsal hemisection. Regeneration of central axons was evaluated after six weeks post-spinal cord injury. During this period, animals received analgesia, and bladder voiding was supported twice daily via gentle abdominal compression. To trace regenerating dorsal column axons, 2 µL of 1% cholera toxin-B (List Biologicals, 103B) was injected into the left sciatic nerve with a 10-µL Hamilton syringe four days before euthanasia. Afterward, animals were perfused with 4% paraformaldehyde, and their spinal cords were post-fixed for one week at 4°C before being cryoprotected in 30% sucrose.

Analysis of microtubule polymerization in DRG explants

DRG ganglia with attached dorsal root (containing central DRG axons) and peripheral nerve (containing peripheral DRG axons) were placed in a 35 mm imaging dish with a glass bottom (#81158, Ibidi). Live imaging recordings were performed in phenol-free neurobasal medium (#12348017, Gibco) supplemented with 2% B27, 2 mM L-glutamine, 1% penicillin–streptomycin, and 50 ng/ml of nerve growth factor. To study microtubule polymerization, imaging of DRG explants from Thy1-EB3-eGFP and spastin knockout and wild-type adult mice was performed using an Andor Revolution XD (Andor Technology) inverted Olympus IX81 (Olympus, UK) spinning disk confocal microscope. An Olympus UPlanLSAPOpo 100x/1.40 Oil immersion objective with a Zeiss Immersol 518F was used. Data was acquired using IQ 2 software (ANDOR Technology, UK). Experiments were conducted in an environmental chamber at 37°C and 5% CO_2. Images were obtained every 2 seconds, for 80 frames, with an exposure time of 200ms, z-range of 6 µm, z-step size of 2 µm, and a final digital resolution of 0.08µm/pixel. For the analysis of microtubule polymerization in DRG explants, only axons with low to moderate expression of eGFP were selected. Four central and peripheral DRG axons in Thy1-EB3-eGFP mice and three central and peripheral DRG axons in spastin knockout and wild-type mice were quantified per animal. The MTrackJ plugin (Meijering et al., 2012) of Fiji/ImageJ software (Schindelin et al., 2012) (RRID:SCR_002285) was used. Gray levels were inverted to facilitate visualization. The velocity of 30 EB3-eGFP comets per axon was quantified during the first 40 frames of each video. To determine the density of polymerizing microtubules, the total number of EB3-eGFP comets contained in an ROI of 100µm^2, during the first 15 frames of each video was quantified.

To analyze total microtubule density, DRG dorsal root, and peripheral nerve were postfixed with 2% osmium tetroxide, dehydrated with ascending series of ethanol, and embedded in Epon. The samples were cut at a thickness of 50 nm and observed using a transmission electron microscope JEOL JEM-1400, at a 40K times magnification and a final resolution of 0.006 µm/pixel. Fiji/ImageJ Cell Counter plugin was used to quantify the total number of microtubules within each axon. Only DRG axons with a diameter between 6-11 µm were quantified. The density of microtubules was obtained by dividing the total number of microtubules by the axonal area. Up to ten axons per DRG branch were quantified.

Immunoblotting

Immunoblots were done on adult naive and sciatic nerve-injured (conditioning lesion) C57BL/6J mice. DRGs from the lumbar roots L3, L4, and L5, which together contribute to the sciatic nerve in this species, were isolated. To minimize contamination from motor axons of the ventral root, a ventral root rhizotomy was performed. Subsequently, the dorsal root (containing DRG central axons) and the peripheral nerve (containing DRG peripheral axons) immediately adjacent to the ganglia were isolated and prepared with ice-cold lysis buffer (1% Triton X-100, 0.1% SDS, 140 mM sodium chloride diluted in Tris-EDTA buffer pH 8.0, and containing protease inhibitors (#04693124001, Roche)). Protein levels were determined using the Detergent Compatible Protein Assay (#5000116, Bio-Rad). 1µg of total protein were used to determine the expression levels of tubulin post-translational modifications and 7.5µg of total protein were used to determine the expression of MAPs. Proteins were loaded onto 4-20% acrylamide gels

(#5671093, Bio-Rad). Gels were transferred to nitrocellulose membranes (#10600013, GE Healthcare Life Sciences), and the primary antibodies were probed overnight at 4°C in 5% bovine serum albumin. The following primary antibodies were used: rat anti-tyrosinated tubulin [YL1/2 (1:5000, #ab6160, Abcam, RRID:AB_305328), mouse anti-acetylated tubulin (1:10.000, #T7451, Sigma-Aldrich, RRID:AB_609894), rabbit anti-Δ2 tubulin (1:2000, #AB3203, Millipore, RRID:AB_177351), rabbit anti-polyglutamylated tubulin (1:10.000, # AG-25B-0030-C050, Adipogen), mouse anti-spastin (1:500, #sc-81624, Santa Cruz, RRID:AB_2286628), rabbit anti-katanin p60 (1:500, #17560-1-AP, ProteinTech, RRID:AB_10694670), mouse anti-tau (1:1000, #4019, Cell Signalling), rat anti-CRMP5 (1:200, #sc-58515, Santa Cruz, RRID:AB_782270), and rabbit anti-vinculin (3:10.000, #700062, Invitrogen). HRP-conjugated secondary antibodies were diluted in 5% skim milk and incubated for 1 hour at room temperature. Membranes were either exposed to Fuji Medical X-Ray Film (#16195209, Fujifilm) and scanned using a Molecular Imager GS800 (Bio-Rad) or directly scanned using a ChemiDoc Imaging System (Bio-Rad). Scanned membranes were quantified using Image Lab software (Bio-Rad, RRID:SCR_014210).

Immunofluorescence of peripheral and central DRG axons

L3, L4 and L5 mouse DRGs were dissected and fixed with 4% paraformaldehyde for 24 hours at 4°C, then transferred into cryoprotection solution and embedded in OCT. Longitudinal sections of 12 µm were prepared using a cryostat and stored at -80°C. The tissues were thawed for 30 minutes at 37ºC and washed three times with PBS to remove all the OCT. Tissue permeabilization was done with 1% triton during 30 minutes

for katanin and with methanol at room temperature for 20 minutes for CRMP5 and tau. Antigen retrieval was performed using Citrate pH 6 for tau and Tris-EDTA pH 9 for CRMP5 and katanin, for 10 minutes at approximately 80-90ºC. Endogenous autofluorescence was blocked with ammonium chloride for 30 minutes, followed by IgG blocking with M.O.M.® blocking reagent (Vecto Laboratories, # MKB-2213) for 1 hour at room temperature. Tissues were further blocked with 5% normal donkey serum for 30 minutes. Primary antibodies, namely rabbit anti-KATNA1 (1:500, Proteintech, # 17560-1-AP), rabbit anti-CRMP5 (1:200, Abcam, #ab36203), mouse anti-tau (1:100, Cell Signalling, #4019), rabbit anti-βIII-tubulin (1:200, Synaptic Systems, #302302), and mouse anti-βIII-tubulin (1:500, Promega, #G7121) were incubated overnight at 4ºC in blocking buffer. The next day, secondary antibodies Alexa Fluor 488 anti-mouse (1:250, Jackson ImmunoResearch, #715-545-15), Alexa Fluor 488 anti-rabbit (1:250, Jackson ImmunoResearch, #711-545-152), Alexa Fluor 594 anti-rabbit (1:250, Jackson ImmunoResearch, #711-585-152), and Alexa Fluor 594 anti-mouse (1:250, Jackson ImmunoResearch, #715-585-150) were incubated in blocking buffer for 1 hour at room temperature. Images were acquired with an inverted Leica SP8 single-point scanning confocal microscope and processed using Leica Application Suite X software. Images were scanned at 400Hz, with a z-step size of 0.5 µm, and a final resolution of 0.15 µm/pixel. To assess fluorescence intensity, mean gray values were measured and background fluorescence was subtracted to obtain the actual fluorescence intensity for each axon.

Analysis of spastin and CRMP5 mRNA in DRG neurons

To assess the levels of spastin and CRMP5 mRNA in DRG central and peripheral axons we performed RNAscope analysis followed by immunohistochemistry as previously described (Li et al., 2021). Of note, considering the size of our target sequences (>300 nucleotides), we were only able to design probes for spastin and CRMP5 using this assay. Briefly, DRGs were dissected and fixed with 4% paraformaldehyde for 24 hours at 4°C, then moved into cryoprotection solution and embedded in OCT. Longitudinal sections of 12 µm were prepared with a cryostat and stored at -80°C. The RNAscope Intro Pack for Multiplex Fluorescent Reagent Kit v2-Mm (#323136, Advanced Cell Diagnostics) was used. Endogenous peroxidases were quenched, antigens were retrieved, and double-Z probes designed for each transcript were hybridized. The HRP signal was developed for each channel, followed by incubation with Opal Dye fluorophores (Opal Dye 520 to label spastin mRNA (#FP1487001KT, Akoya) and Opal Dye 620 to label CRMP5 mRNA (#FP1495001KT, Akoya)). Immunohistochemistry was performed immediately after the RNAscope. Slides were blocked with 10% donkey serum. The primary antibody rabbit anti-myelin basic protein (1:1000, #10458-1-AP, Proteintech, RRID:AB_2250289) was incubated overnight, followed by the secondary antibody Alexa Fluor 647 anti-Rabbit (1:500, #711-605-152, Jackson ImmunoResearch, RRID:AB_2492288) for 1 hour at room temperature. Samples were imaged using an inverted Leica SP8 single-point scanning confocal microscope and acquired using the Leica Application Suit X software. Spastin and CRMP5 mRNA puncta were quantified using Fiji/ImageJ Cell Counter, and the total axonal mRNA density was determined by dividing the number of mRNA puncta per

image area. Three non-consecutive peripheral and central DRG sections per animal were quantified.

Immunofluorescence of DRG neuron cultures

DRG neurons from E16 Wistar rats at DIV 21 were fixed with pre-warmed 2% PFA diluted in PHEM buffer (65mM PIPES, 25 mM HEPES, 10 mM EGTA, 3 mM MgCl2, and 0.1% Triton X-100, pH of 6.9) for 20 minutes. Endogenous autofluorescence and IgG were blocked with ammonium chloride and M.O.M.® blocking reagent (# MKB-2213, Vecto Laboratories, RRID:AB_2336587) respectively. Primary antibodies rabbit anti-polyglutamate chain (1:1000, # AG-25B-0030-C050, Adipogen), mouse anti-acetylated tubulin (1:500, #T7451, Sigma-Aldrich), rabbit anti-Δ2 tubulin (1:1000, #AB3203, Millipore), rabbit anti-βIII-tubulin (1:1000, #302302, Synaptic Systems, RRID:AB_10637424) and mouse anti-βIII-tubulin (1:1000, #G7121, Promega, RRID:AB_430874) were incubated overnight, followed by incubation with the secondary antibodies Alexa Fluor 594 anti-Mouse (1:500, #715-585-150, Jackson ImmunoResearch, RRID:AB_2340854), Alexa Fluor 488 anti-Rabbit (1:500, #711-545-152, Jackson ImmunoResearch, RRID:AB_2313584), Alexa Fluor 594 anti-Rabbit (1:500, #A21207, Invitrogen), Alexa Fluor 647 anti-Rabbit (1:500, # 711-605-152, Jackson ImmunoResearch), and DAPI staining. Images were acquired with an inverted Leica SP5 single-point scanning confocal microscope using Leica LasAF software (version 2.6.3.8173), with a pinhole size of 102.9 µm, calculated at 1 AU for 580 nm emission, and a z-step size of 0.3 µm with a final resolution of 0.24 µm/pixel. We assessed the fluorescence intensity of polyglutamylated, acetylated, Δ2 tubulin, and

βIII-tubulin at the large and thin axons in a region of 10 µm from the T-junction. This analysis was conducted using ImageJ/Fiji software by calculating their mean gray values, with background fluorescence intensity subtracted. PTMs mean gray values were normalized against βIII-tubulin mean gray values. Eight pseudo-unipolar DRG neurons were quantified per independent experiment. Representative images of various developmental stages of DRG neurons were captured using the inverted Leica SP8 single-point scanning confocal microscope. Images were scanned at 400Hz, with a final resolution of 0.28 µm/pixel.

Analysis of regeneration of dorsal column tract axons

Serial sagittal sections of the spinal cord (50 µm) from non-injured mice, spinal cord-injured mice, and mice where the spinal cord injury was preceded by a sciatic nerve injury (conditioning group) were collected for immunofluorescence against cholera toxin-B. The sections were blocked and incubated overnight with goat anti-cholera toxin-B primary antibody (1:30.000, #703, List Biologicals, RRID:AB_10013220), followed by incubation with biotinylated horse anti-goat antibody (1:200, #BA-9500, Vector Laboratories, RRID:AB_2336123) and Alexa Fluor 568-streptavidin (1:1000, #S11226, Invitrogen, RRID:AB_2315774). Cell nuclei were stained with DAPI, and the tissue was imaged using an IN Cell Analyzer 2000 automated microscope (GE Healthcare) in DAPI and FITC channels to visualize nuclei and cholera toxin-B-positive axons, respectively. Mosaics of a single spinal cord were stitched using the IN Cell Developer Toolbox (GE Healthcare) software. Lesion borders were delineated based on nuclei alignment—organized outside the lesion but disordered within the injured area—and further

corroborated by cholera toxin-B staining, as most injured central DRG axons halt their growth at the lesion site. To measure the number of regenerating dorsal column tract axons, the lesion border was outlined and the number of cholera toxin-B- positive axons growing inside the lesion area were counted using the Fiji/ImageJ Cell Counter plugin. Were analyzed up to six spinal cord sections per animal. The fluorescence intensity of cholera toxin-B-positive axons was quantified using ImageJ/Fiji software by calculating the mean gray value in different spinal cord sections. Were analyzed up to six spinal cord sections per animal.

Analysis of myelinated and unmyelinated axons in spastin knockout animals

The sciatic nerve of spastin knockout mice and wild-type littermates were postfixed with 2% osmium tetroxide and embedded in Epon. For the analysis of myelinated axons, cross-sections at 500 nm were stained with 1% paraphenylenediamine (PPD) and mounted in dibutylphthalate polystyrene xylene (DPX). The entire area of the nerve was imaged using an Olympus optical microscope (Olympus, Japan) equipped with an Olympus DP 25 camera, a 40x / 0.17 objective, and Cell B software (Olympus, Japan). Mosaics with a resolution of 0.08 µm/pixel were stitched in Photoshop (Adobe, USA, RRID:SCR_014199), using the command Photomerge. The Fiji/ImageJ Cell Counter plugin was used to measure the density of myelinated axons. For the analysis of unmyelinated axons, samples were cut at a thickness of 50 nm. Images were acquired using the transmission electron microscope JEOL JEM-1400 (JEOL, Japan) and digitally recorded using a CCD digital camera Orius 1100W (Gatan, USA), with an 8K times magnification and a final resolution of 0.006 µm/pixel. The Fiji/ImageJ Cell

Counter plugin was used to determine the density of unmyelinated axons. Only unmyelinated axons inside Remak bundles were used for quantification. A total of twelve non-overlapping images per animal were quantified.

Culture of adult DRG neurons on aggrecan

Culture of adult DRG neurons was performed following the protocol described in (Fleming et al., 2009). Briefly, DRGs from the lumbar root L3, L4 and L5 of adult spastin knockout mice and wild-type littermates were isolated, freed of roots, and digested with 0.125% collagenase-IV-S (Sigma, C1889) for 90 minutes at 37°C with 5% CO_2. After enzymatic digestion, the DRGs were mechanically dissociated using fire-polished Pasteur pipettes of decreasing diameters. The cells were dissociated in culture media consisting of DMEM:F12 (Sigma, D8437) supplemented with 1x B27, 1% penicillin-streptomycin, 2 mM L-glutamine, and 50 ng/mL NGF. To separate neurons from glial cells, the dissociated cells were centrifuged in a 15% BSA (Sigma, A3294) gradient for 10 minutes at 200 g. The neuron-containing pellet was then seeded at 5,000 neurons per well in 24-well plates pre-coated with 20 µg/mL poly-L-lysine and 5 µg/mL laminin:20 µg/mL aggrecan (Sigma, A1960). Cultures were maintained at 37°C in a 5% CO_2 incubator and fixed in pre-warmed 2% PFA at DIV1. Immunofluorescence for βIII-tubulin was performed as described above. Imaging was conducted using a Leica DMI6000 widefield inverted motorized microscope (Leica Microsystems, Germany) equipped with a Hamamatsu FLASH4.0 camera (Hamamatsu, Japan). Samples were excited at 460/40 nm, with an exposure time of 500 ms. Leica Las X software was used for image acquisition, and all images were saved as LIF files with a final resolution of

0.31 µm/pixel. Tiles were acquired and merged using the smooth blend option. The merged images were converted to Imaris files, and the Filaments tool was used to reconstruct and analyze the neurites by performing automatic tracing. To ensure the accuracy of each traced neuron, we manually refined and edited the automatically traced filaments to reduce errors. Five wild-type and five spastin knockout merged images, containing between 10-40 neurons each, were quantified. The number of primary neurites was obtained through Sholl analysis.

Statistical analysis

Depending on the sample size, the normality of the datasets was tested using the Shapiro-Wilk or D'Agostino-Pearson omnibus normality test. If data followed a normal distribution, a two-tailed Student's t-test, one-way or two-way ANOVA were used. The Student t-test was applied only for comparisons between two groups; a paired t-test was used when two variables were measured in a single subject. For multiple comparisons where a single independent variable is present, we utilized one-way ANOVA. Repeated measures were applied when multiple measurements were taken from the same neuron. Two-way ANOVA was used whenever two independent variables were present. ANOVA were followed by a Fisher's Least Significant Difference (LSD) post-hoc test. For the data that did not follow a normal distribution, a Wilcoxon matched pair or a Mann-Whitney U nonparametric test was used. The chi-square test was applied to compare categorical data. The statistical details, including the statistical test used in each experiment, the exact value of *n*, what *n* represents, the number of animals and the number of independent experiments used, can be found in the figure legends. All statistical tests

and data visualization were performed using GraphPad Prism 8 (GraphPad, RRID:SCR_002798), with results presented as mean ± standard error of the mean (SEM). P-values were represented by asterisks, where **** $P \leq 0.0001$, *** $P \leq 0.001$, ** $P \leq 0.01$, * $P \leq 0.05$, and non-significant (ns) $P > 0.05$.

Acknowledgements

We thank the i3S Advanced Light Microscopy, Histology, Electron Microscopy and BioSciences Screening (PT-OPENSCREEN NORTE-01-0145-FEDER-085468) platforms, all part of PPBI (POCI-01-0145-FEDER-022122). We also thank the i3S Animal and the Cell Culture and Genotyping facilities. We thank the Advanced Imaging Unit at Instituto Gulbenkian de Ciência (PPBI-POCI-01-0145-FEDER-022122/ LISBOA-01-0246-FEDER-000037_SingleCell). We are grateful to Sandra Braz for her assistance with performing spinal cord injuries. Illustrations are by Rita Sousa Costa (Aparas Design Lab). This work was funded by national funds through Foundation for Science and Technology (FCT), under the project DRI/India/0336/2020, SFRH/BD/143926/2019, and COVID/BD/153330/2023), the German Research Foundation (GRK1459; KN556/11-1; ID 450131873; TRR 274/1 2020), the Deutsche Gesellschaft für Muskelkranke (LE 4610/1-1), the German Center for Neurodegenerative Diseases, and SyNergy Cluster (EXC 2145; ID 390857198).

Author contributions

M.M. Sousa coordinated the study. A.C. Costa, T. Misgeld, M.S.Brill, and M.M. Sousa conceptualized it. A.C. Costa performed most experiments and analyses. B.R. Murillo, R. Bessa, R. Ribeiro, and T. Ferreira da Silva provided experimental support. P. Porfírio-Rodrigues and G.G. Martins assisted with laser axotomy. P. Brites and M. Kneussel provided conceptual support in experiments involving the spastin knockout mouse. A.C. Costa and M.M. Sousa wrote the manuscript with input from all authors.

References

Ahmad, F.J., W. Yu, F.J. Mcnally and P.W. Baas. 1999. An essential role for katanin in severing microtubules in the neuron. *J Cell Biol.* 145**:**305-15.

Banker, G. 2018. The Development of Neuronal Polarity: A Retrospective View. *J Neurosci.* 38**:**1867-1873.

Bisby, M.A. 1981. Axonal transport in the central axon of sensory neurons during regeneration of their peripheral axon. *Neurosci Lett.* 21**:**7-11.

Bodakuntla, S., A.S. Jijumon, C. Villablanca, C. Gonzalez-Billault and C. Janke. 2019. Microtubule-Associated Proteins: Structuring the Cytoskeleton. *Trends Cell Biol.* 29**:**804-819.

Brill, M.S., T. Kleele, L. Ruschkies, M. Wang, N.A. Marahori, M.S. Reuter, T.J. Hausrat, E. Weigand, M. Fisher, A. Ahles, S. Engelhardt, D.L. Bishop, M. Kneussel and T. Misgeld. 2016. Branch-Specific Microtubule Destabilization Mediates Axon Branch Loss during Neuromuscular Synapse Elimination. *Neuron.* 92**:**845-856.

Cengiz, N., G. Ozturk, E. Erdogan, A. Him and E.K. Oguz. 2012. Consequences of neurite transection in vitro. *J Neurotrauma.* 29**:**2465-74.

Chen, K., Y. Ye, Z. Ji, M. Tan, S. Li, J. Zhang, G. Guo and H. Lin. 2014. Katanin p60 promotes neurite growth and collateral formation in the hippocampus. *Int J Clin Exp Med.* 7**:**2463-70.

Dunn, S., E.E. Morrison, T.B. Liverpool, C. Molina-Paris, R.A. Cross, M.C. Alonso and M. Peckham. 2008. Differential trafficking of Kif5c on tyrosinated and detyrosinated microtubules in live cells. *J Cell Sci.* 121**:**1085-95.

Erturk, A., F. Hellal, J. Enes and F. Bradke. 2007. Disorganized microtubules underlie the formation of retraction bulbs and the failure of axonal regeneration. *J Neurosci.* 27**:**9169-80.

Fleming, C.E., F.M. Mar, F. Franquinho, M.J. Saraiva and M.M. Sousa. 2009. Transthyretin internalization by sensory neurons is megalin mediated and necessary for its neuritogenic activity. *J Neurosci.* 29**:**3220-32.

Fukata, Y., T.J. Itoh, T. Kimura, C. Menager, T. Nishimura, T. Shiromizu, H. Watanabe, N. Inagaki, A. Iwamatsu, H. Hotani and K. Kaibuchi. 2002. CRMP-2 binds to tubulin heterodimers to promote microtubule assembly. *Nat Cell Biol.* 4**:**583-91.

Garcia-Anoveros, J., T.A. Samad, L. Zuvela-Jelaska, C.J. Woolf and D.P. Corey. 2001. Transport and localization of the DEG/ENaC ion channel BNaC1alpha to peripheral mechanosensory terminals of dorsal root ganglia neurons. *J Neurosci.* 21**:**2678-86.

Giorgi, S., A. Lamberti, L. Butron, O. Gross-Amat, D. Alarcon-Alarcon, E. Rodriguez-Canas, A. Fernandez-Carvajal and A. Ferrer-Montiel. 2023. Compartmentalized primary cultures of dorsal root ganglion neurons to model peripheral pathophysiological conditions. *Mol Pain.* 19**:**17448069231197102.

Gornstein, E.L. and T.L. Schwarz. 2017. Neurotoxic mechanisms of paclitaxel are local to the distal axon and independent of transport defects. *Exp Neurol.* 288**:**153-166.

Gumy, L.F., E.A. Katrukha, I. Grigoriev, D. Jaarsma, L.C. Kapitein, A. Akhmanova and C.C. Hoogenraad. 2017. MAP2 Defines a Pre-axonal Filtering Zone to Regulate

KIF1- versus KIF5-Dependent Cargo Transport in Sensory Neurons. *Neuron.* 94**:**347-362 e7.

Ha, H. 1970. Axonal bifurcation in the dorsal root ganglion of the cat: a light and electron microscopic study. *J Comp Neurol.* 140**:**227-40.

Hellal, F., A. Hurtado, J. Ruschel, K.C. Flynn, C.J. Laskowski, M. Umlauf, L.C. Kapitein, D. Strikis, V. Lemmon, J. Bixby, C.C. Hoogenraad and F. Bradke. 2011. Microtubule stabilization reduces scarring and causes axon regeneration after spinal cord injury. *Science.* 331**:**928-31.

Hoffman, P.N. 2010. A conditioning lesion induces changes in gene expression and axonal transport that enhance regeneration by increasing the intrinsic growth state of axons. *Exp Neurol.* 223**:**11-8.

Hou, S.T. 2020. The regulatory and enzymatic functions of CRMPs in neuritogenesis, synaptic plasticity, and gene transcription. *Neurochem Int.* 139**:**104795.

Iwanski, M.K. and L.C. Kapitein. 2023. Cellular cartography: Towards an atlas of the neuronal microtubule cytoskeleton. *Front Cell Dev Biol.* 11**:**1052245.

Janke, C. and M.M. Magiera. 2020. The tubulin code and its role in controlling microtubule properties and functions. *Nat Rev Mol Cell Biol.* 21**:**307-326.

Ji, Z., G. Zhang, L. Chen, J. Li, Y. Yang, C. Cha, J. Zhang, H. Lin and G. Guo. 2018. Spastin Interacts with CRMP5 to Promote Neurite Outgrowth by Controlling the Microtubule Dynamics. *Dev Neurobiol.* 78**:**1191-1205.

Jin, Z., H.F. Shou, J.W. Liu, S.S. Jiang, Y. Shen, W.Y. Cheng and L.L. Gao. 2022. Spastin interacts with CRMP5 to promote spindle organization in mouse oocytes by severing microtubules. *Zygote.* 30**:**80-91.

Kadavath, H., R.V. Hofele, J. Biernat, S. Kumar, K. Tepper, H. Urlaub, E. Mandelkow and M. Zweckstetter. 2015. Tau stabilizes microtubules by binding at the interface between tubulin heterodimers. *Proc Natl Acad Sci U S A.* 112**:**7501-6.

Kapitein, L.C., M.A. Schlager, W.A. Van Der Zwan, P.S. Wulf, N. Keijzer and C.C. Hoogenraad. 2010. Probing intracellular motor protein activity using an inducible cargo trafficking assay. *Biophys J.* 99**:**2143-52.

Katano, T., T. Mabuchi, E. Okuda-Ashitaka, N. Inagaki, T. Kinumi and S. Ito. 2006. Proteomic identification of a novel isoform of collapsin response mediator protein-2 in spinal nerves peripheral to dorsal root ganglia. *Proteomics.* 6**:**6085-94.

Kleele, T., P. Marinkovic, P.R. Williams, S. Stern, E.E. Weigand, P. Engerer, R. Naumann, J. Hartmann, R.M. Karl, F. Bradke, D. Bishop, J. Herms, A. Konnerth, M. Kerschensteiner, L. Godinho and T. Misgeld. 2014. An assay to image neuronal microtubule dynamics in mice. *Nat Commun.* 5**:**4827.

Komiya, Y. 1981. Axonal regeneration in bifurcating axons of rat dorsal root ganglion cells. *Exp Neurol.* 73**:**824-6.

Komiya, Y. and M. Kurokawa. 1978. Asymmetry of protein transport in two branches of bifurcating axons. *Brain Res.* 139**:**354-8.

Koseki, H., M. Donega, B.Y. Lam, V. Petrova, S. Van Erp, G.S. Yeo, J.C. Kwok, C. Ffrench-Constant, R. Eva and J.W. Fawcett. 2017. Selective rab11 transport and the intrinsic regenerative ability of CNS axons. *Elife.* 6.

Kuo, Y.W. and J. Howard. 2021. Cutting, Amplifying, and Aligning Microtubules with Severing Enzymes. *Trends Cell Biol.* 31**:**50-61.

Lacroix, B., J. Van Dijk, N.D. Gold, J. Guizetti, G. Aldrian-Herrada, K. Rogowski, D.W. Gerlich and C. Janke. 2010. Tubulin polyglutamylation stimulates spastin-mediated microtubule severing. *J Cell Biol.* 189**:**945-54.

Li, X., S. Eadara, S. Jeon, Y. Liu, G. Muwanga, L. Qu, M.J. Caterina and M.K. Meffert. 2021. Combined single-molecule fluorescence in situ hybridization and immunohistochemistry analysis in intact murine dorsal root ganglia and sciatic nerve. *STAR Protoc.* 2**:**100555.

Mar, F.M., A. Bonni and M.M. Sousa. 2014a. Cell intrinsic control of axon regeneration. *EMBO Rep.* 15**:**254-63.

Mar, F.M., A.R. Simoes, S. Leite, M.M. Morgado, T.E. Santos, I.S. Rodrigo, C.A. Teixeira, T. Misgeld and M.M. Sousa. 2014b. CNS axons globally increase axonal transport after peripheral conditioning. *J Neurosci.* 34**:**5965-70.

Matsuda, S., N. Kobayashi, K. Mominoki, H. Wakisaka, M. Mori and S. Murakami. 2000. [Morphological transformation of sensory ganglion neurons and satellite cells]. *Kaibogaku Zasshi.* 73**:**603-13.

Meijering, E., O. Dzyubachyk and I. Smal. 2012. Methods for cell and particle tracking. *Methods Enzymol.* 504**:**183-200.

Nascimento, A.I., T.F. Da Silva, E.C. Fernandes, L.L. Luz, F.M. Mar, B.V. Safronov and M.M. Sousa. 2022. Sensory neurons have an axon initial segment that initiates spontaneous activity in neuropathic pain. *Brain.* 145**:**1632-1640.

Nascimento, A.I., F.M. Mar and M.M. Sousa. 2018. The intriguing nature of dorsal root ganglion neurons: Linking structure with polarity and function. *Prog Neurobiol.* 168**:**86-103.

Neumann, S. and C.J. Woolf. 1999. Regeneration of dorsal column fibers into and beyond the lesion site following adult spinal cord injury. *Neuron.* 23**:**83-91.

Nirschl, J.J., A.E. Ghiretti and E.L.F. Holzbaur. 2017. The impact of cytoskeletal organization on the local regulation of neuronal transport. *Nat Rev Neurosci.* 18**:**585-597.

Panda, D., B.L. Goode, S.C. Feinstein and L. Wilson. 1995. Kinetic stabilization of microtubule dynamics at steady state by tau and microtubule-binding domains of tau. *Biochemistry.* 34**:**11117-27.

Papasozomenos, S.C., L.I. Binder, P.K. Bender and M.R. Payne. 1985. Microtubule-associated protein 2 within axons of spinal motor neurons: associations with microtubules and neurofilaments in normal and beta,beta'-iminodipropionitrile-treated axons. *J Cell Biol.* 100**:**74-85.

Pero, M.E., C. Meregalli, X. Qu, G.J. Shin, A. Kumar, M. Shorey, M.M. Rolls, K. Tanji, T.H. Brannagan, P. Alberti, G. Fumagalli, L. Monza, W.B. Grueber, G. Cavaletti and F. Bartolini. 2021. Pathogenic role of delta 2 tubulin in bortezomib-induced peripheral neuropathy. *Proc Natl Acad Sci U S A.* 118.

Perry, G.W. and D.L. Wilson. 1981. Protein synthesis and axonal transport during nerve regeneration. *J Neurochem.* 37**:**1203-17.

Richardson, P.M. and V.M. Verge. 1987. Axonal regeneration in dorsal spinal roots is accelerated by peripheral axonal transection. *Brain Res.* 411**:**406-8.

Roll-Mecak, A. and R.D. Vale. 2008. Structural basis of microtubule severing by the hereditary spastic paraplegia protein spastin. *Nature.* 451**:**363-7.

Schindelin, J., I. Arganda-Carreras, E. Frise, V. Kaynig, M. Longair, T. Pietzsch, S. Preibisch, C. Rueden, S. Saalfeld, B. Schmid, J.Y. Tinevez, D.J. White, V. Hartenstein, K. Eliceiri, P. Tomancak and A. Cardona. 2012. Fiji: an open-source platform for biological-image analysis. *Nat Methods.* 9**:**676-82.

Siahaan, V., J. Krattenmacher, A.A. Hyman, S. Diez, A. Hernandez-Vega, Z. Lansky and M. Braun. 2019. Kinetically distinct phases of tau on microtubules regulate kinesin motors and severing enzymes. *Nat Cell Biol.* 21**:**1086-1092.

Song, A.H., D. Wang, G. Chen, Y. Li, J. Luo, S. Duan and M.M. Poo. 2009. A selective filter for cytoplasmic transport at the axon initial segment. *Cell.* 136**:**1148-60.

Stepanova, T., J. Slemmer, C.C. Hoogenraad, G. Lansbergen, B. Dortland, C.I. De Zeeuw, F. Grosveld, G. Van Cappellen, A. Akhmanova and N. Galjart. 2003. Visualization of microtubule growth in cultured neurons via the use of EB3-GFP (end-binding protein 3-green fluorescent protein). *J Neurosci.* 23**:**2655-64.

Stone, G.C. and D.L. Wilson. 1979. Qualitative analysis of proteins rapidly transported in ventral horn motoneurons and bidirectionally from dorsal root ganglia. *J Neurobiol.* 10**:**1-12.

Suh, Y.S., K. Chung and R.E. Coggeshall. 1984. A study of axonal diameters and areas in lumbosacral roots and nerves in the rat. *J Comp Neurol.* 222**:**473-81.

Szczesna, E., E.A. Zehr, S.W. Cummings, A. Szyk, K.K. Mahalingan, Y. Li and A. Roll-Mecak. 2022. Combinatorial and antagonistic effects of tubulin glutamylation and glycylation on katanin microtubule severing. *Dev Cell.* 57**:**2497-2513 e6.

Tan, D., H. Zhang, J. Deng, J. Liu, J. Wen, L. Li, X. Wang, M. Pan, X. Hu and J. Guo. 2020. RhoA-GTPase Modulates Neurite Outgrowth by Regulating the Expression of Spastin and p60-Katanin. *Cells.* 9.

Tan, R., A.J. Lam, T. Tan, J. Han, D.W. Nowakowski, M. Vershinin, S. Simo, K.M. Ori-Mckenney and R.J. Mckenney. 2019. Microtubules gate tau condensation to spatially regulate microtubule functions. *Nat Cell Biol.* 21**:**1078-1085.

Tas, R.P., A. Chazeau, B.M.C. Cloin, M.L.A. Lambers, C.C. Hoogenraad and L.C. Kapitein. 2017. Differentiation between Oppositely Oriented Microtubules Controls Polarized Neuronal Transport. *Neuron.* 96**:**1264-1271 e5.

Valenstein, M.L. and A. Roll-Mecak. 2016. Graded Control of Microtubule Severing by Tubulin Glutamylation. *Cell.* 164**:**911-21.

Vikman, K.S., E. Backstrom, K. Kristensson and R.H. Hill. 2001. A two-compartment in vitro model for studies of modulation of nociceptive transmission. *J Neurosci Methods.* 105**:**175-84.

Wujek, J.R. and R.J. Lasek. 1983. Correlation of axonal regeneration and slow component B in two branches of a single axon. *J Neurosci.* 3**:**243-51.

Zala, D., M.V. Hinckelmann, H. Yu, M.M. Lyra Da Cunha, G. Liot, F.P. Cordelieres, S. Marco and F. Saudou. 2013. Vesicular glycolysis provides on-board energy for fast axonal transport. *Cell.* 152**:**479-91.

Zehr, E., A. Szyk, G. Piszczek, E. Szczesna, X. Zuo and A. Roll-Mecak. 2017. Katanin spiral and ring structures shed light on power stroke for microtubule severing. *Nat Struct Mol Biol.* 24**:**717-725.

Zheng, Y., J. Wildonger, B. Ye, Y. Zhang, A. Kita, S.H. Younger, S. Zimmerman, L.Y. Jan and Y.N. Jan. 2008. Dynein is required for polarized dendritic transport and uniform microtubule orientation in axons. *Nat Cell Biol.* 10**:**1172-80.

Figures

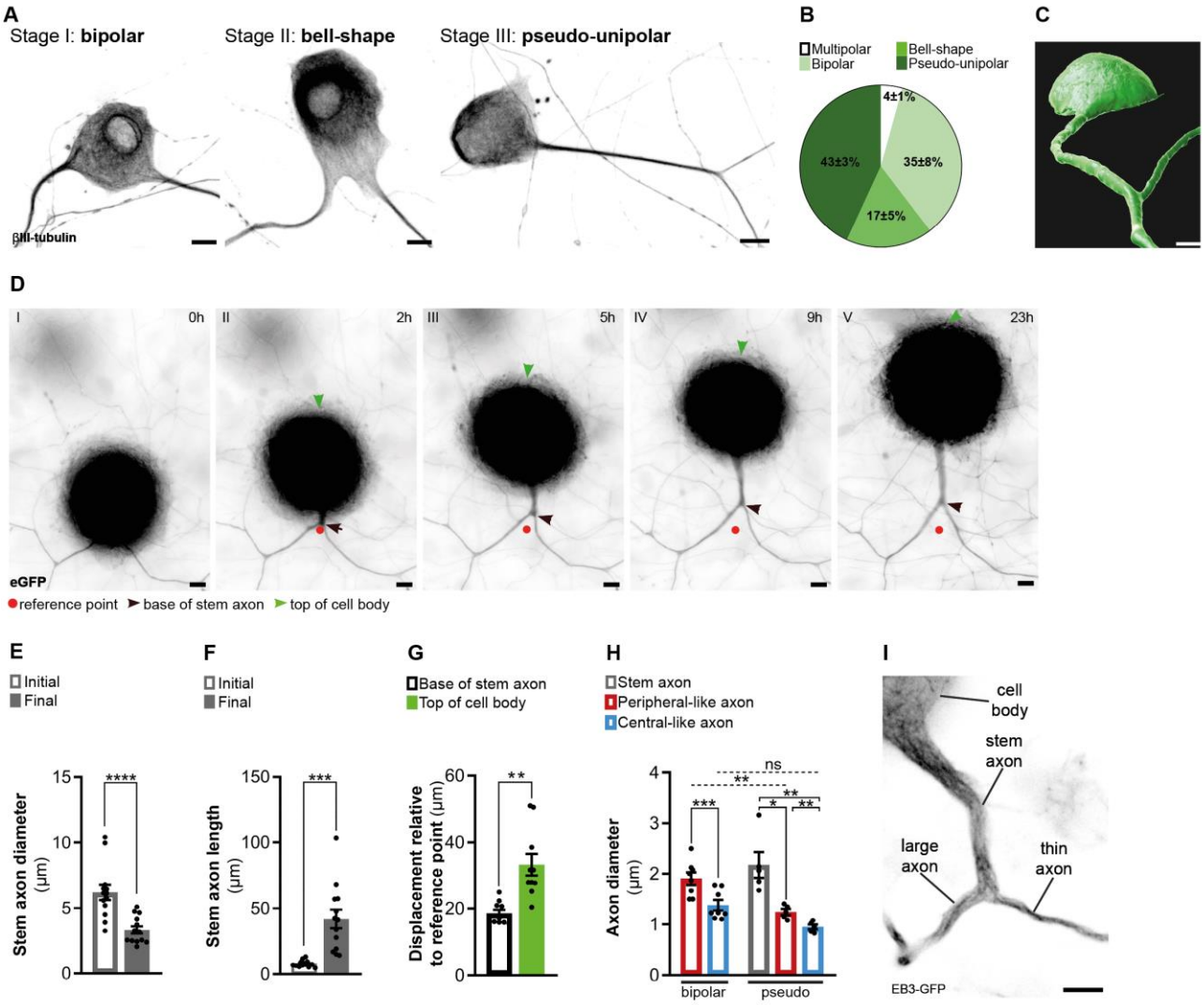

Figure 1. *In vitro* DRG neurons recapitulate *in vivo* developmental stages. (A) *In vitro* DRG neurons labeled with βIII-tubulin depicting different development stages. Scale bar, 10 µm. **(B)** Percentage of different DRG neuron morphologies at DIV21 (n= 3 independent experiments, 100 cells per experiment). **(C)** Imaris segmentation of a pseudo-unipolar DRG neuron transduced with AAV-CMV-eGFP. Scale bar, 7 µm. **(D)** *In vitro* DRG neurons transduced with AAV-CMV-eGFP depicting stem axon formation. Scale bar, 10 µm. **(E-F)** Stem axon diameter (D) and length (E) of DRG neuron axons

from the formation of the stem axon (Initial) to the final stage of pseudo-unipolarization (Final) (n= 13 neurons; paired t-test, diameter ****p<0.0001, length ***p=0.0004). **(G)** Stem axon and cell-body displacement during pseudo-unipolarization (n= 13 neurons; paired t-test, **p=0.0020). **(H)** *In vitro* diameter of DRG axons; n= 5-8 independent experiments, 5-10 neurons/experiment; paired t-test in bipolar neurons, ***p=0.0003; repeated measures (RM) one-way ANOVA in pseudo-unipolar neurons, stem-peripheral *p=0.0196, stem-central **p=0.0069, peripheral-central **p=0.0048; for comparisons amongst peripheral and central-like axons from bipolar and pseudo-unipolar neurons, a two-way ANOVA was used (peripheral: **p=0.0039; central: p=0.9829). (**I**) *In vitro* pseudo-unipolar DRG neuron transduced with the lentivirus CMV-EB3-GFP depicting different axon diameter. Scale bar, 5 µm. Data are represented as mean ± SEM.

Figure 1 – video 1. Segmentation of an *in vitro* pseudo-unipolar embryonic rat DRG neuron expressing eGFP.

Figure 1 – video 2. *In vitro* embryonic rat DRG neurons assembling a stem axon.

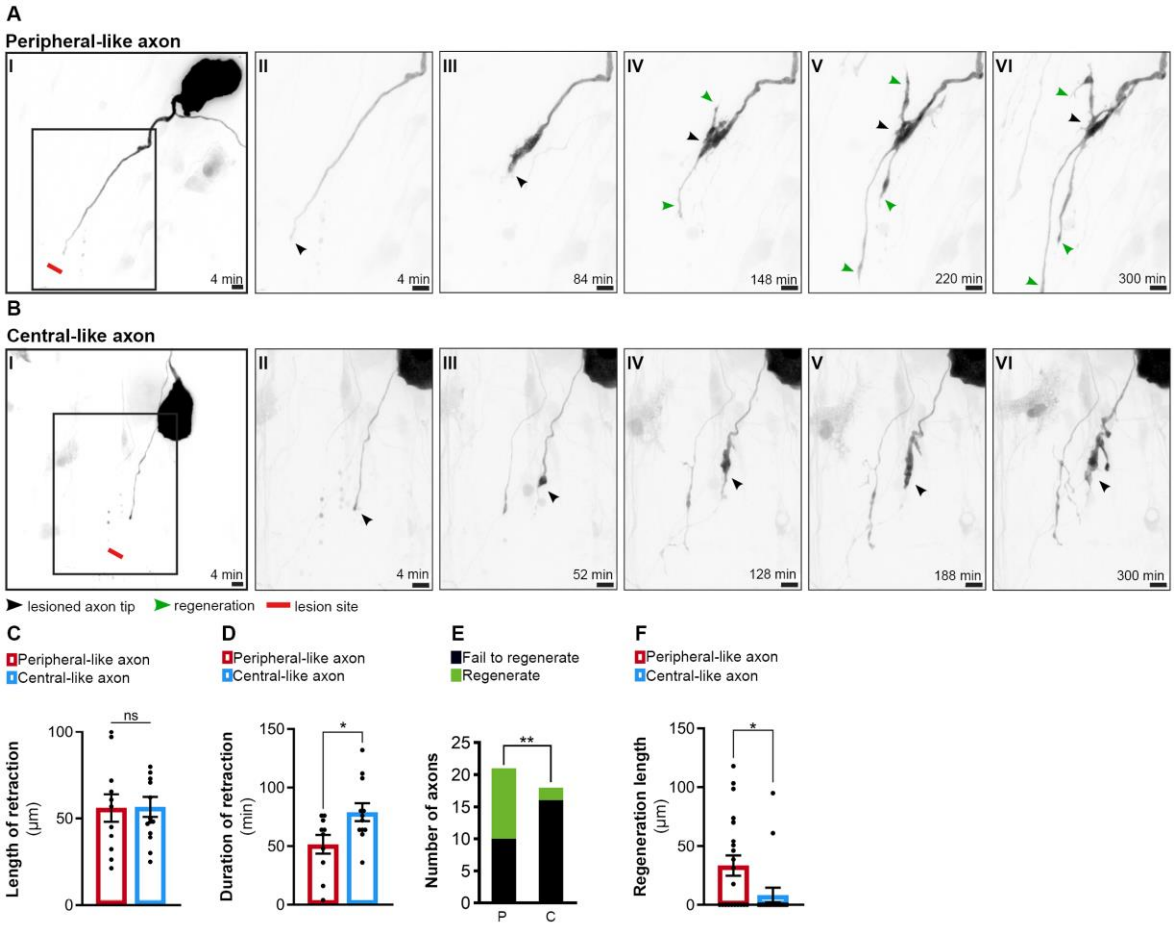

Figure 2. *In vitro* DRG neurons recapitulate *in vivo* regenerative asymmetry. (A-B) Live imaging of *in vitro* regeneration of a peripheral-like (A) and a central-like axon (B). Scale bar, 10 µm. The injury sites are marked by red lines; lesioned axon tips by black arrowheads and regenerating axons by green arrowheads. **(C-D)** Length (C) and duration (D) of axon retraction after laser axotomy (n= 10-14 axons, 3 independent experiments; unpaired t-test, length p=0.9541, duration *p=0.0228). **(E)** Number of regenerating and non-regenerating peripheral-like (P) and central-like (C) DRG axons. The chi-square test was used (5 independent experiments, **p=0.0082). **(F)** Regeneration length of peripheral and central-like axons following laser axotomy (n= 18-

21 axons, 5 independent experiments; unpaired t-test, *p=0.0297). Data are represented as mean ± SEM.

Figure 2 – video 1. Laser axotomy of peripheral and central-like rat DRG axons.

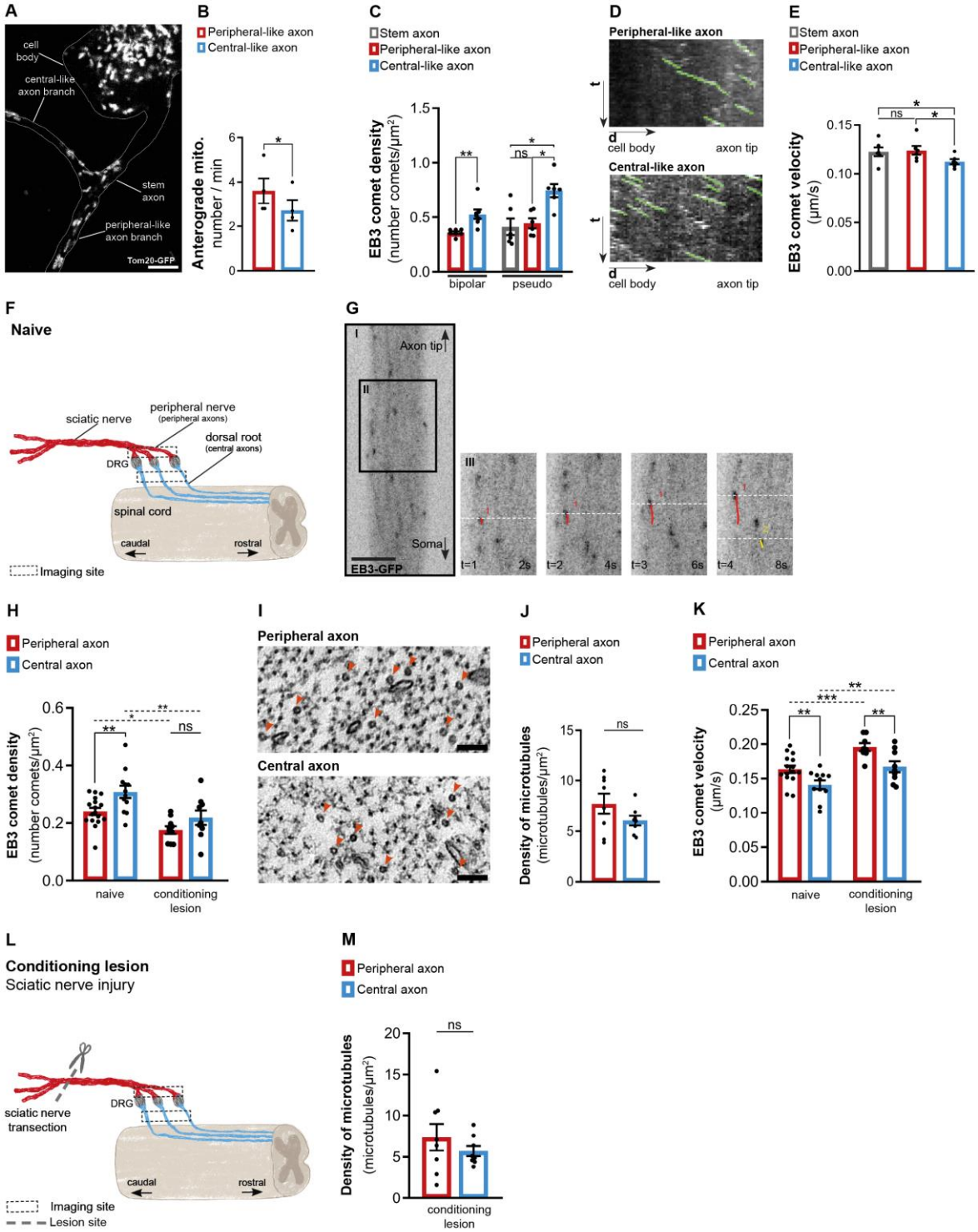

Figure 3. DRG axons display asymmetric microtubule polymerization, attenuated by a conditioning lesion. (A) *In vitro* pseudo-unipolar DRG neuron transduced with a Tom20-GFP lentivirus, labelling mitochondria. Scale bar, 5 µm. **(B)** Quantification of the

anterograde mitochondria flux (n=4 independent experiments, 5 DRGs/experiment; paired t-test, *p=0.0143). **(C)** EB3-GFP comet density in *in vitro* DRG axons (n= 6-7 independent experiments, 5-10 neurons/experiment; paired t-test in bipolar axons, **p=0.0038; RM one-way ANOVA in pseudo-unipolar axons, stem-central *p=0.0221, peripheral-central *p=0.0171. **(D)** Kymographs of *in vitro* pseudo-unipolar DRG axons. **(E)** EB3-GFP comet velocity in *in vitro* pseudo-unipolar DRG axons (n= 6 independent experiments, 5-10 neurons/experiment; RM one-way ANOVA, stem-central *p=0.0443, peripheral-central *p=0.0183). **(F)** Representation of naive DRG neurons connected to the peripheral nerve (containing peripheral axons) and dorsal root (containing central axons). The dashed squares indicates the imaging locations. **(G)** Live imaging of DRG axons from Thy1-EB3-eGFP mice. Scale bar, 5 µm. **(H)** EB3-GFP comet density in DRG explants from naive mice (n= 12-17 animals; 3-6 axons/animal, **p=0.0037) and mice with a peripheral conditioning lesion (CL) (n=9-10 animals, 3-5 axons/animal, p=0.1423). Two-way ANOVA; peripheral naive-peripheral CL, *p=0.0276; central naive-central CL, **p=0.0026. **(I)** High magnification electron microscopy images within individual naive DRG axons, depicting axonal microtubules (red arrowheads). Scale bar, 100 nm. **(J)** Total density of microtubules in naive DRG axons (n= 8 animals, 5-10 axons/animal; paired t-test, p=0.2299). **(K)** EB3-GFP comet velocity in DRG explants from naive mice (n=11-15 animals, 3-6 axons/animal, **p=0.0048) and mice with peripheral CL (n=8-9 animals, 3-5 axons/animal, **p=0.0035). Two-way ANOVA, peripheral naive-peripheral CL, ***p=0.0003; central naive-central CL, **p=0.0038. **(L)** Representation of a sciatic nerve injury to DRG neurons (conditioning lesion). The dashed square indicates the imaging location, while the dashed line and scissor marks

the lesion site. **(M)** Total density of axonal microtubules in DRG peripheral and central axons after peripheral CL (n= 8 animals, 5 axons/animal; paired t-test, p=0.4624). Data are represented as mean ± SEM.

Figure 3 – video 1. Mitochondria transport in *in vitro* DRG neurons.

Figure 3 – video 2. Microtubule dynamics in *in vitro* DRG neurons.

Figure 3 – video 3. Microtubule dynamics in *in vivo* DRG neurons.

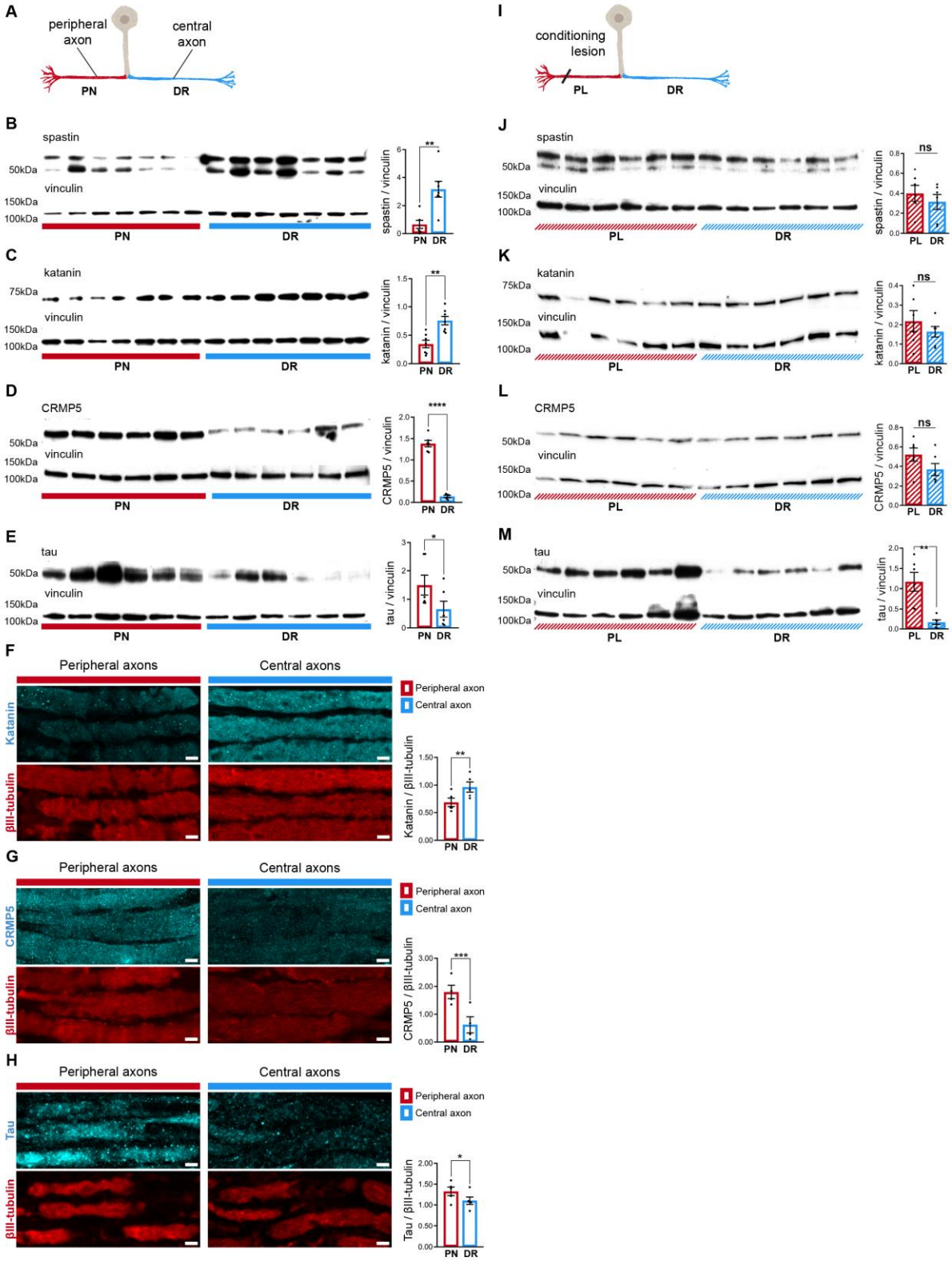
A
peripheral axon
central axon
PN
DR
B
spastin
50kDa
vinculin
150kDa
100kDa
PN
DR
spastin / vinculin
**
C
katanin
75kDa
vinculin
150kDa
100kDa
katanin / vinculin
**
D
CRMP5
50kDa
vinculin
150kDa
100kDa
CRMP5 / vinculin
****
E
tau
50kDa
vinculin
150kDa
100kDa
tau / vinculin
*
F
Peripheral axons
Central axons
Katanin
βIII-tubulin
Peripheral axon
Central axon
Katanin / βIII-tubulin
**
G
Peripheral axons
Central axons
CRMP5
βIII-tubulin
Peripheral axon
Central axon
CRMP5 / βIII-tubulin
***
H
Peripheral axons
Central axons
Tau
βIII-tubulin
Peripheral axon
Central axon
Tau / βIII-tubulin
*
I
conditioning lesion
PL
DR
J
spastin
50kDa
vinculin
150kDa
100kDa
PL
DR
spastin / vinculin
ns
K
katanin
75kDa
vinculin
150kDa
100kDa
katanin / vinculin
ns
L
CRMP5
50kDa
vinculin
150kDa
100kDa
CRMP5 / vinculin
ns
M
tau
50kDa
vinculin
150kDa
100kDa
tau / vinculin
**

1165

Figure 4. DRG axons have a distinctive MAP signature that adapts upon conditioning lesion. (A) Representation of a naive DRG neuron. Peripheral axons within the peripheral nerve (PN) are depicted in red and central axons within the dorsal root (DR) in blue. **(B-E)** Western blot analysis of the PN and DR (n= 5-7 animals) and respective quantification of (B) spastin (unpaired t-test, **p=0.0032), (C) katanin (paired t-test, **p=0.0063), (D) CRMP5 (unpaired t-test, ****p<0.0001), and (E) tau (Wilcoxon test, *p=0.0313) levels. **(F-H)** Immunofluorescence of (F) katanin and βIII-tubulin, (G) CRMP5 and βIII-tubulin, and (H) tau and βIII-tubulin in DRG axons (n= 4-5 animals) and respective quantification (katanin, paired t-test, **p=0.0021; CRMP5, paired t-test, ***p=0.009; tau, paired t-test, *p= 0.0114). Scale bar, 5 µm. **(I)** Representation of a DRG neuron with a priming peripheral lesion (peripheral lesion- PL). **(J-M)** Western blot of DRG peripheral nerve and dorsal root following PL (n= 6 animals) and respective quantification (n= 6 animals; paired t-test) showing (J) spastin (p=0.4085), (K) katanin (p=0.2661), (L) CRMP5 (p=0.1326) and (M) tau (**p=0.0052) levels. Data are represented as mean ± SEM.

Figure 4 – source data 1. PTMs western blots original files.

Figure 4 – source data 2. PTMs western blots with the relevant bands clearly labelled.

Figure 4 – source data 3. MAPs western blots original files.

Figure 4 – source data 4. MAPs western blots with the relevant bands clearly labelled.

Figure 4 – figure supplement 1. Peripheral and central DRG axons show similar levels of tubulin post-translational modifications.

Figure 4 – figure supplement 2. Potential Sorting Mechanism at the DRG T-Junction.

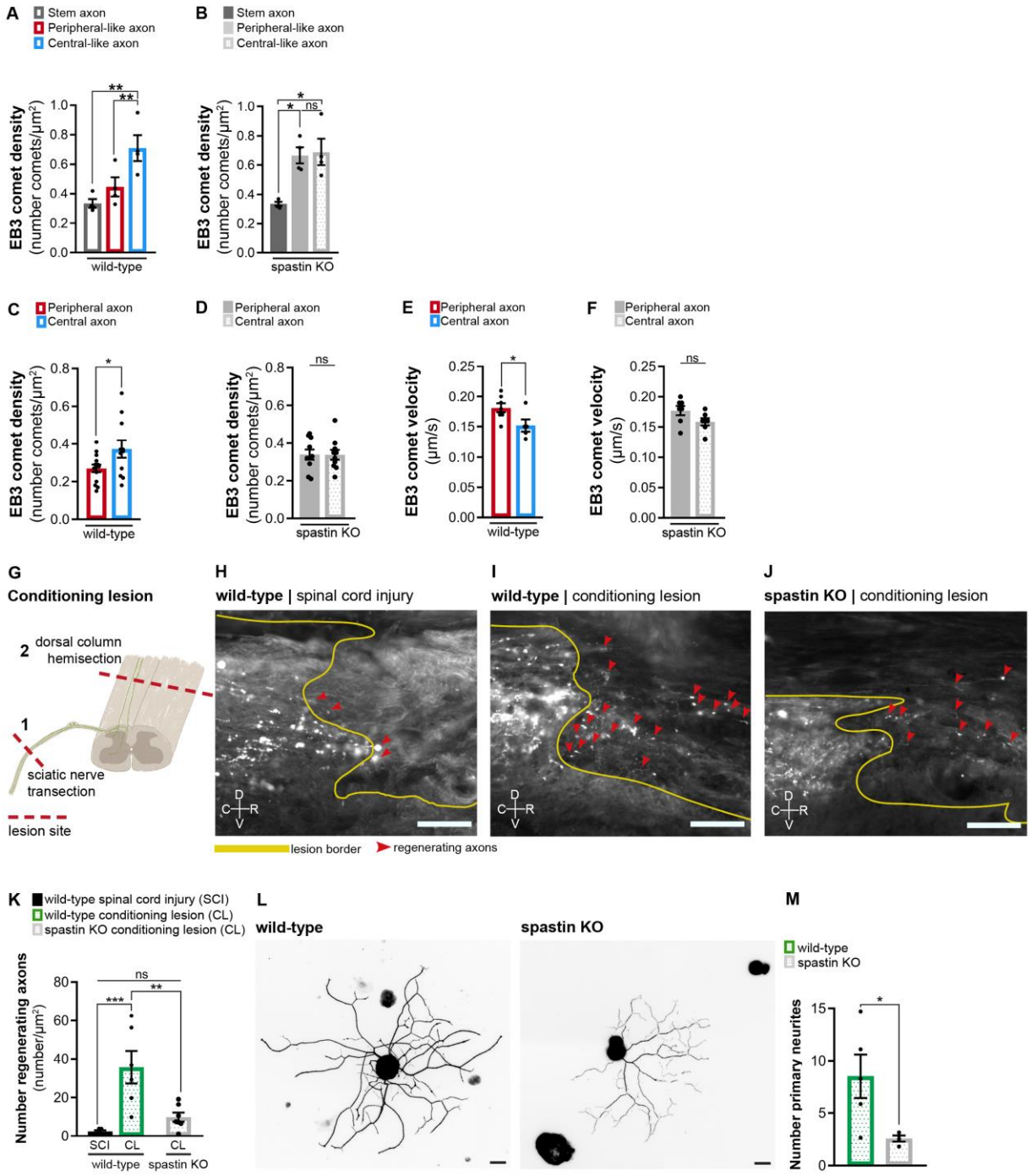

Figure 5. Spastin deficiency is sufficient to abolish the asymmetry of DRG axons. **(A)** Density of EB3-GFP comets in wild-type DRG axons *in vitro* (n= 4 independent experiments, 10 cells/experiment; RM one-way ANOVA, stem-peripheral p= 0.0536, stem-central **p= 0.0082, peripheral-central **p= 0.0027). **(B)** Density of EB3-GFP

comets in spastin knock-out DRG axons *in vitro* (n= 4 independent experiments, 10 cells/experiment; RM one-way ANOVA, stem-peripheral *p= 0.0168, stem-central *p= 0.0250, peripheral-central p= 0.8762). **(C-D)** EB3-eGFP comet density in (C) wild-type and (D) spastin knock-out mice (n= 10-14 animals; 3 axons/animal; unpaired t-test; wild-type, *p=0.0388; knock-out, p=0.9792). **(E-F)** EB3-eGFP comet velocity in (E) wild-type and (F) spastin knock-out mice (n= 5-7 animals; 3 axons/animal; unpaired t-test; wild-type, *p=0.0405; knock-out, p=0.0823). **(G)** Representation of the conditioning lesion (CL). A dorsal column hemisection is preceded by a sciatic nerve transection 1 week before. Lesion sites are indicated with dashed red lines and DRG axons in green. **(H-J)** Longitudinal spinal cord sections of (H) wild-type mice with spinal cord lesion or (I) CL and (J) spastin knockout mice with CL. Dorsal column tract axons were traced with cholera toxin-B (white). The lesion border is highlighted by a yellow line. Regenerating axons are highlighted by red arrowheads. C-caudal; R-rostral; D-dorsal; V-ventral. Scale bar, 100 µm. **(K)** Number of regenerating axons in wild-type mice with spinal cord injury (n= 5 animals) and CL (n= 6 animals), and spastin knockout with CL (n= 7 animals); 6 sections per animal. One-way ANOVA; wild-type SCI-CL, ***p=0.0005; wild-type-knockout CL, **p=0.0020; wild-type SCI-knockout CL, p=0.3335. **(L)** Representative *in vitro* wild-type and spastin knockout adult DRG neurons labeled with βIII-tubulin. Scale bar, 30 µm. **(M)** Quantification of the number of primary neurites in adult wild-type and spastin knockout DRG neurons. n= 4-5 independent experiments for wild-type and spastin knockout; unpaired t-test; *p= 0.0205. Data are represented as mean ± SEM.

Figure 5 – figure supplement 1. Signs of axon degeneration are not observed in 15 weeks old spastin knockout animals.

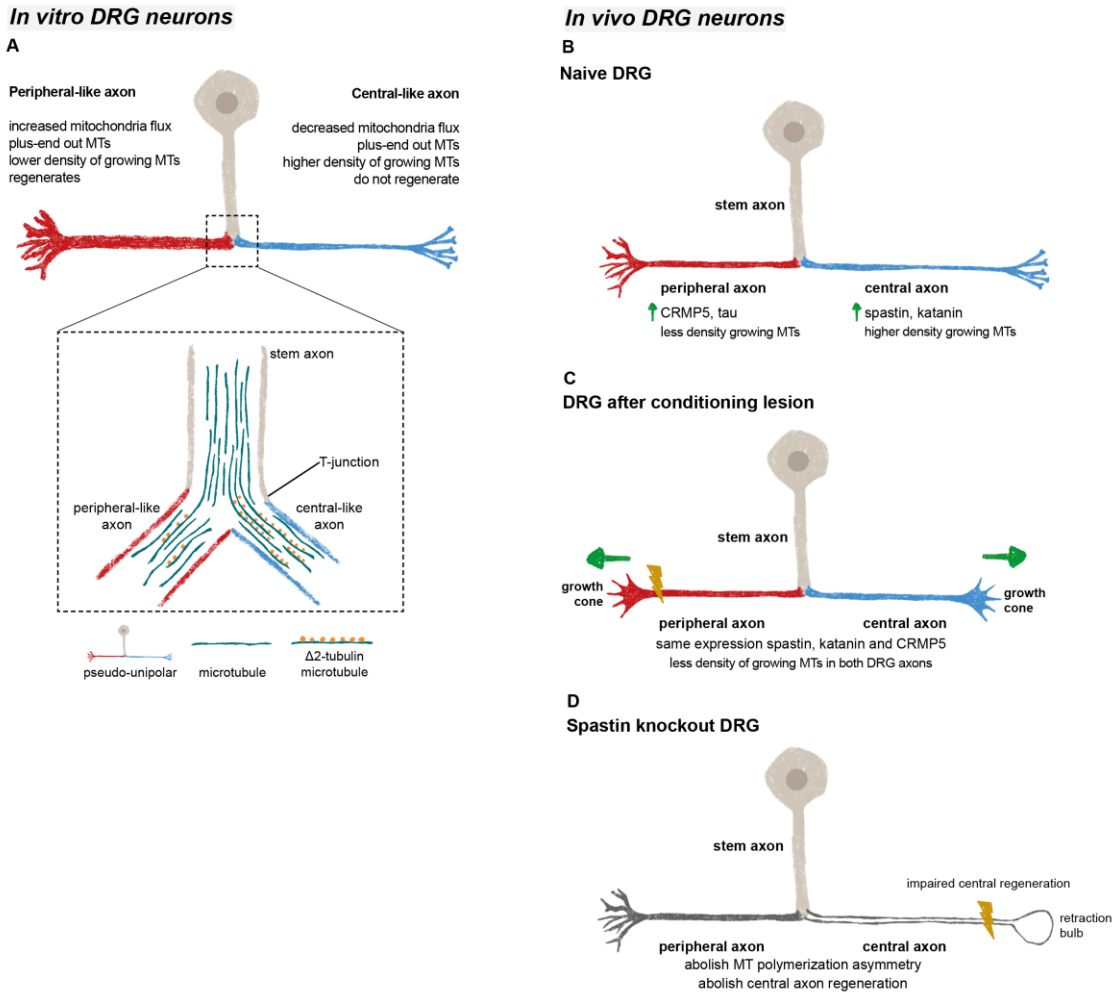

Figure 6. Microtubules in DRG axons are distinctively regulated both *in vivo* and *in vitro*. (A) *In vitro* DRG cultures replicate *in vivo* asymmetry in microtubule polymerization (established already at the bipolar stage) and reveal a potential cargo filtering mechanism operating at the DRG T-junction, where a higher continuum of microtubules from the stem axon to the central-like axonal branch is found, together with increased levels of Δ2 tubulin in the central-like axonal branch. **(B)** Under physiological conditions, peripheral DRG axons show a decreased density of growing microtubules when compared to central axons due to an asymmetric MAP signature. **(C)** After a peripheral conditioning lesion, the DRG axon MAP signature is remodeled,

leading to a decrease in the density of growing microtubules and regeneration of both peripheral and central axons. **(D)** Perturbing the DRG MAP signature by knocking out spastin, abolishes DRG axon asymmetry and central axon regeneration following conditioning lesion.

Supplemental Figures

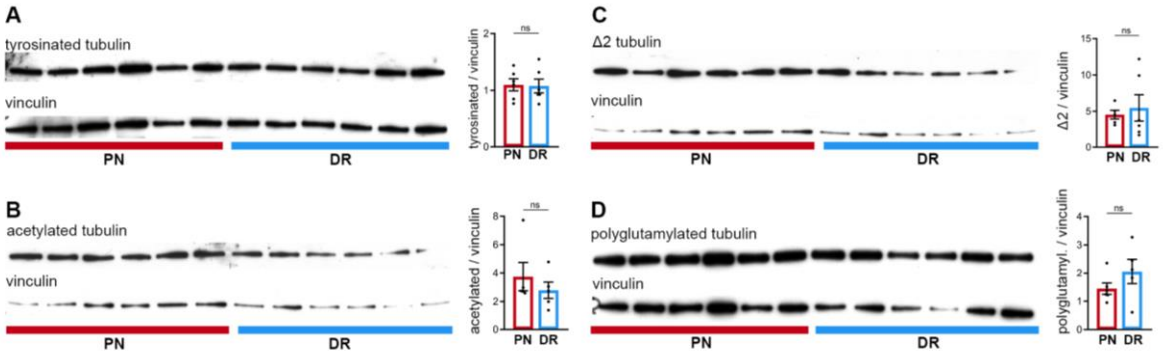

Figure 4 – figure supplement 1. Peripheral and central DRG axons show similar levels of tubulin post-translational modifications. (A-D) Western blot analysis of DRG peripheral nerve (PN) and dorsal root (DR) and respective quantification of (A) tyrosinated tubulin (n= 6 animals; paired t-test, p=0.9075), (B) acetylated tubulin (n= 5 animals; Mann-Whitney U test, p=0.7302), (C) Δ2 tubulin (n= 5-6 animals; unpaired t-test, p=0.6639), and (D) polyglutamylated tubulin (n= 5-6 animals; unpaired t-test, , p=0.2052) expression levels. Data are represented as mean ± SEM.

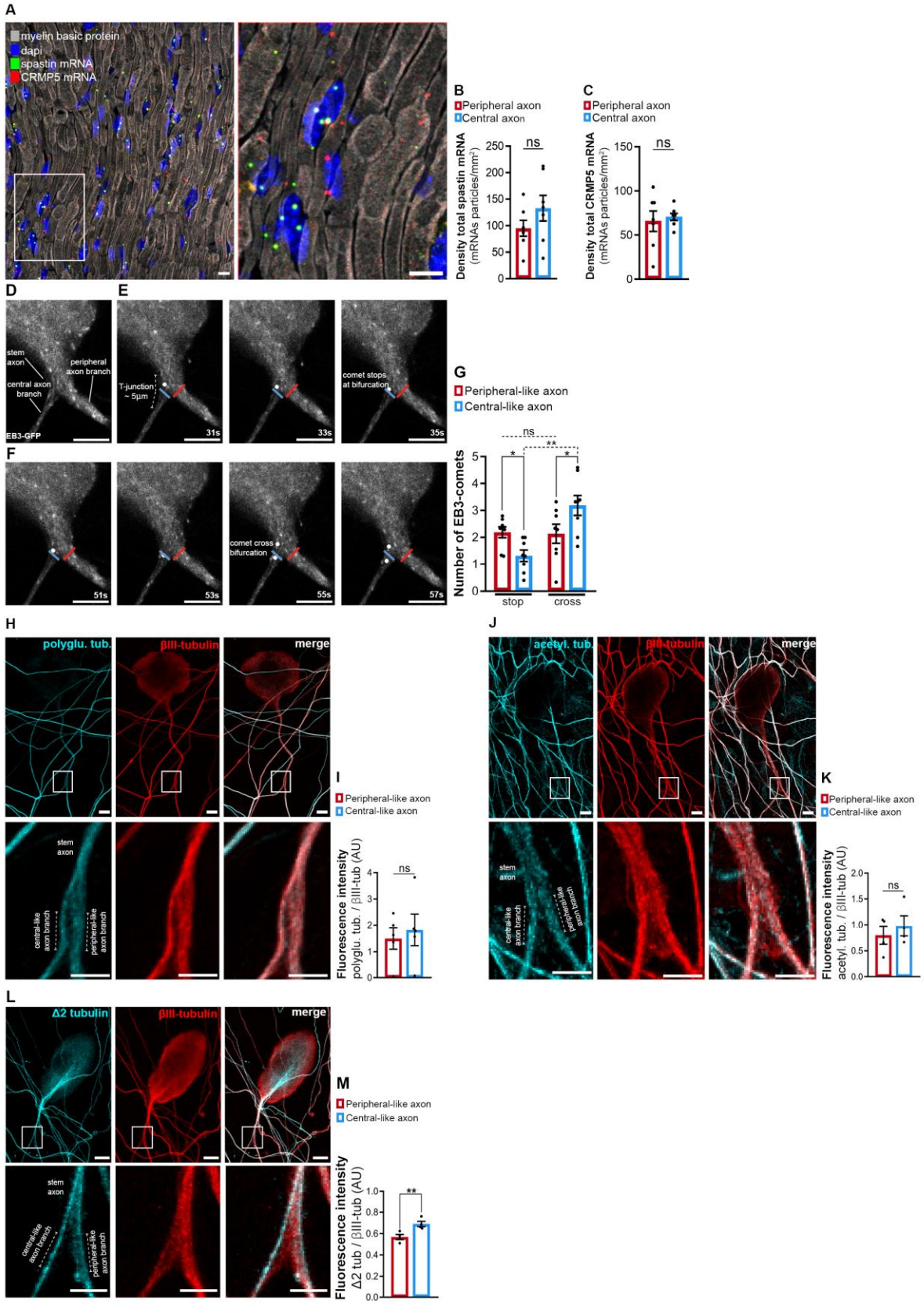
A
myelin basic protein
dapi
spastin mRNA
CRMP5 mRNA
B
Peripheral axon
Central axon
Density total spastin mRNA (mRNAs particles/mm²)
ns
C
Peripheral axon
Central axon
Density total CRMP5 mRNA (mRNAs particles/mm²)
ns
D
stem axon
peripheral axon branch
central axon branch
EB3-GFP
E
T-junction ~ 5µm
31s
33s
comet stops at bifurcation
35s
F
51s
53s
comet cross bifurcation
55s
57s
G
Peripheral-like axon
Central-like axon
Number of EB3-comets
ns
*
**
*
stop
cross
H
polyglu. tub.
βIII-tubulin
merge
stem axon
central-like axon branch
peripheral-like axon branch
I
Peripheral-like axon
Central-like axon
Fluorescence intensity polyglu. tub. / βIII-tub (AU)
ns
J
acetyl. tub.
βIII-tubulin
merge
stem axon
central-like axon branch
peripheral-like axon branch
K
Peripheral-like axon
Central-like axon
Fluorescence intensity acetyl. tub. / βIII-tub (AU)
ns
L
Δ2 tubulin
βIII-tubulin
merge
stem axon
central-like axon branch
peripheral-like axon branch
M
Peripheral-like axon
Central-like axon
Fluorescence intensity Δ2 tub / βIII-tub (AU)
**

1268

Figure 4 – figure supplement 2. Potential Sorting Mechanism at the DRG T-Junction. (A) Representative images of a peripheral DRG axon after performing RNAscope analysis to detect spastin and CRMP5 mRNA particles. Scale bar, 10 µm. **(B-C)** The density of (B) total spastin mRNA and (C) total CRMP5 mRNA in the DRG peripheral nerve and dorsal root (n= 7 animals, 3 non-consecutive DRG peripheral nerve and dorsal root sections were analyzed per animal). Paired t-test, spastin: p=0.2112, CRMP5 p=0.7671. **(D)** *In vitro* pseudo-unipolar DRG neurons transduced with a CMV-EB3-GFP lentivirus. Scale bar, 5 µm. (E-F) Sequential images of EB3-GFP comets, either stopping (E) or crossing (F) the DRG T-junction. This analysis spanned a 5 µm region from the end of the DRG stem axon to the start of either the peripheral-like (red line) or central-like (blue line) axonal branch. Scale bar, 5 µm. (G) Number of EB3-GFP comets that either stop or cross the DRG-T junction (n=8 independent experiments, 10 DRGs/experiment; RM two-way ANOVA, stop *p=0.0439, cross *p=0.0162, stop-cross peripheral p= 0.9169, stop-cross central **p=0.0032). **(H)** Immunofluorescence of polyglutamylated tubulin and βIII-tubulin in DRG peripheral and central like axonal branches. Scale bar, 10 µm, and close-up 5 µm. **(I)** Quantification of polyglutamylated tubulin fluorescence intensity normalized to βIII-tubulin (n=5 independent experiments, 8 pseudo-unipolar DRGs per experiment, paired t-test, p= 0.2957). **(J)** Immunofluorescence of acetylated tubulin and βIII-tubulin in DRG peripheral and central like axonal branches. Scale bar, 10 µm, and close-up 5 µm. **(K)** Quantification of acetylated tubulin fluorescence intensity normalized to βIII-tubulin (n=4 independent experiments, 8 pseudo-unipolar DRGs per experiment, paired t-test, p= 0.2946). **(L)** Immunofluorescence of Δ2 tubulin and βIII-tubulin in DRG peripheral and

central like axonal branches. Scale bar, 10 µm, and close-up 5 µm. **(M)** Quantification of Δ2 tubulin fluorescence intensity (n=4 independent experiments, 8 DRGs/experiment; paired t-test, **p= 0.0012). Data are represented as mean ± SEM.

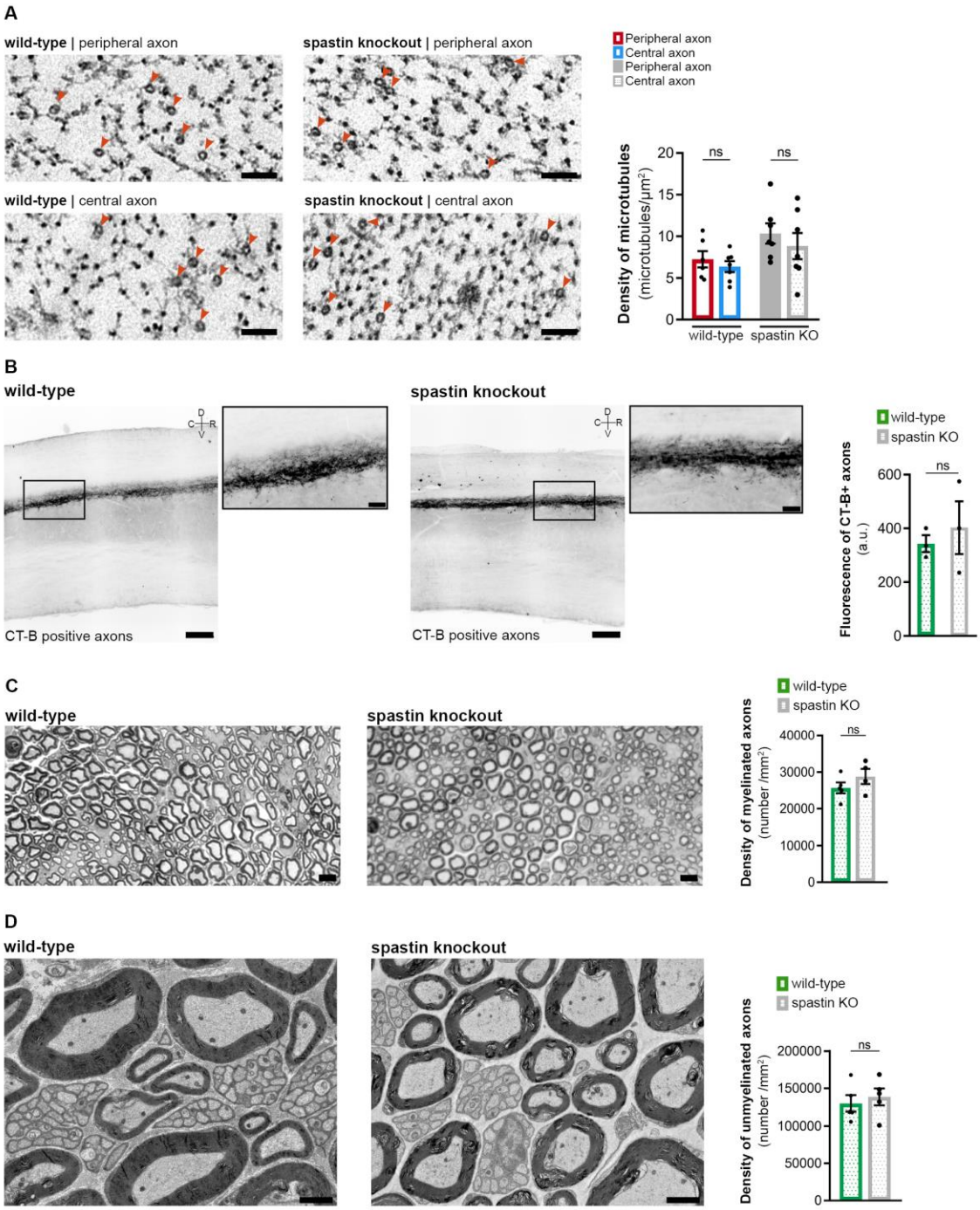

Figure 5 – figure supplement 1. Signs of axon degeneration are not observed in 15 weeks old spastin knockout animals. (A) Representative electron microscopy images (left) and respective quantification (right) of the total density of axonal

microtubules in wild-type and spastin knockout peripheral and central DRG axons (n= 6-7 animals, up to 10 axons/animal). Two-way ANOVA followed by Fisher's LSD post hoc test, p=0.6030 wild-type peripheral-central axons and p=0.3615 spastin knockout peripheral-central axons. **(B)** Representative images (left) of the dorsal column tract central axons of naive 15 weeks old wild-type and spastin knockout animals traced with cholera toxin-B (black) injection (zoom-ins of boxed regions are provided; Scale bars: 200 µm and 50 µm in zoom-ins) and respective quantification (n=3 animals; up to 6 spinal cord sections analyzed per animal; unpaired t-test, p=0.5918) (right). **(C)** Representative images of sciatic nerve semi-thin sections of naive 15 weeks old wild-type and spastin knockout animals (left; scale bar, 10 µm) and respective quantification of myelinated axons (n=4-5 animals, all myelinated axons in a complete nerve cross-section were quantified; unpaired t-test, p=0.2455) (right). **(D)** Representative electron microscopy images of the sciatic nerve of naive 15 weeks old wild-type and spastin knockout animals (left; scale bar, 2 µm) and respective quantification of unmyelinated axons (n=5 animals, unmyelinated axons inside Remak bundles were quantified; paired t-test, p=0.6315) (right). Data are represented as mean ± SEM.

Videos

Figure 1 - Video 1. Segmentation of an *in vitro* pseudo-unipolar embryonic rat DRG neuron expressing eGFP. Segmentation of an *in vitro* pseudo-unipolar embryonic rat DRG neuron expressing eGFP acquired using timelapse confocal microscopy. An Imaris Surfaces tool was applied to extract a 3D object from the DRG neuron outer contour, using an intensity threshold to distinguish cell from the background. Scale bar, variable throughout the video. Related to Figure 1C.

Figure 1 - Video 2. *In vitro* embryonic DRG neurons assembling a stem axon. Timelapse epifluorescence microscopy showing *in vitro* embryonic rat DRG neurons assembling a stem axon from a bipolar bell-shape DRG morphology into a pseudo-unipolar morphology at early (DIV 7-14, left) and late (DIV 14-21, right) DIVs. To identify their morphology, neurons express eGFP. Images were acquired every hour and play at 2.7×10^{-4} frames per second. Scale bar, 10 µm. Related to Figure 1D.

Figure 2 - Video 1. Laser axotomy of peripheral and central-like DRG axons. Timelapse spinning-disk confocal microscopy showing an *in vitro* pseudo-unipolar embryonic rat DRG neuron expressing eGFP. Peripheral-like and central-like axonal branches were injured 100-200 µm from the DRG T-junction with a 355 nm pulsed lased at a maximum of 50% laser power. Images were acquired every 4 minutes. The video plays at 4.1×10^{-3} frames per second. Scale bar, 10 µm. Related to Figure 2A-B.

Figure 3 - Video 1. Mitochondria transport in *in vitro* DRG neurons.Timelapse confocal microscopy showing an *in vitro* pseudo-unipolar embryonic rat DRG neuron expressing Tom20-GFP to assess mitochondria axonal transport (white dots). Images were acquired every 2 seconds. The video plays at 0.5 frames per second. Scale bar, 5 µm. Related to Figure 3A.

Figure 3 - Video 2. Microtubule dynamics in *in vitro* DRG neurons. Timelapse confocal microscopy showing an *in vitro* pseudo-unipolar embryonic rat DRG neuron expressing EB3-GFP (dark dots) to assess microtubule dynamics. Images were acquired every 2 seconds. The video plays at 0.5 frames per second. Scale bar, 5 µm. Related to Figure 3C-E.

Figure 3 - Video 3. Microtubule dynamics in *in vivo* DRG neurons. Timelapse spinning-disk confocal microscopy showing *in vivo* adult peripheral and central DRG axons from Thy1-EB3-eGFP mice. The axon expresses EB3-eGFP (dark dots) to assess microtubule dynamics. Images were acquired every 2 seconds. The video plays at 0.5 frames per second. Scale bar, 5 µm. Related to Figure 3G.

1389 ## Key Resources Table

Key Resources Table				
Reagent type (species) or resource	**Designation**	**Source or reference**	**Identifiers**	**Additional information**
strain, strain background (*R. norvegicus*)	Wistar rats	Charles River	Strain Code 003	
strain, strain background (*M. musculus*)	C57BL/6	Charles River	Strain Code 027 RRID:MGI:2159769	
strain, strain background (*M. musculus*)	Thy1-EB3-eGFP	From Thomas Misgeld Group		
strain, strain background (*M. musculus*)	Spastin knockout	From Matthias Kneussel Group		
transfected construct (*M. musculus*)	Lentivirus CMV-EB3-GFP	Plasmid from Frank Polleux		Lentiviral construct to transduce DRG cells with EB3-GFP.
transfected construct (*M. musculus*)	AAVPHP.S-CMV-eGFP	VectorBuilder	Cat# VB010000-9394npt	AAV construct to transduce DRG cells with eGFP.
transfected construct (*M. musculus*)	Lentivirus synapsin-Tom20-GFP	Charité NeuroCure, University of Berlin	Cat# BLV-569a	Lentiviral construct to transduce DRG cells

				with Tom20-GFP.
antibody	anti-tyrosinated tubulin [YL1/2] (Rat monoclonal)	Abcam	Cat# ab6160 RRID:AB_305328	WB (1:5000)
antibody	anti-acetylated tubulin (mouse monoclonal)	Sigma-Aldrich	Cat# T7451 RRID:AB_609894	WB (1:10000)
antibody	anti-Δ2 tubulin (rabbit polyclonal)	Millipore	Cat# AB3203 RRID:AB_177351	IF cells (1:1000) WB (1:2000)
antibody	anti-polyglutamylated tubulin (rabbit polyclonal)	Adipogen	Cat# AG-25B-0030-C050	IF cells (1:1000) WB (1:10000)
antibody	anti-spastin (mouse monoclonal)	Santa Cruz	Cat# sc-81624 RRID:AB_2286628	WB (1:500)
antibody	anti-katanin p60 (rabbit polyclonal)	ProteinTech	Cat# 17560-1-AP RRID:AB_10694670	IF tissue (1:500) WB (1:500)
antibody	anti-tau (mouse monoclonal)	Cell Signalling	Cat# 4019	IF tissue (1:100) WB (1:1000)
antibody	anti-CRMP5 (rat monoclonal)	Santa Cruz	Cat# sc-58515 RRID:AB_782270	IF tissue (1:200) WB (1:200)

antibody	anti-vinculin (rabbit monoclonal)	Invitrogen	Cat# 700062	WB (3:10000)
antibody	anti-CT-B primary (goat)	List Biologicals	Cat# 703 RRID:AB_10013220	IF tissue (1:30000)
antibody	Biotinylated horse anti-goat	Vector Laboratories	Cat# BA-9500 RRID:AB_2336123	IF tissue (1:30000)
antibody	anti-myelin basic protein (rabbit polyclonal)	Proteintech	Cat# 10458-1-AP RRID:AB_2250289	IF tissue (1:1000)
antibody	anti-βIII-tubulin (rabbit polyclonal)	Synaptic Systems	Cat# 302302 RRID:AB_10637424	IF tissue (1:200) IF cells (1:1000)
antibody	anti-βIII-tubulin (mouse monoclonal)	Promega	Cat# G7121 RRID:AB_430874	IF tissue (1:500) IF cells (1:1000)
antibody	Alexa Fluor 647 anti-(rabbit)	Jackson ImmunoResearch	Cat# 711-605-152 RRID:AB_2492288	IF tissue and cells (1:500)
antibody	Alexa Fluor 594 anti-(mouse)	Jackson ImmunoResearch	Cat# 715-585-150 RRID:AB_2340854	IF tissue (1:250) IF cells (1:500)
antibody	Alexa Fluor 488 anti-(rabbit)	Jackson ImmunoResearch	Cat# 711-545-152 RRID:AB_2313584	IF tissue (1:250) IF cells (1:500)

antibody	Alexa Fluor 594 anti-(rabbit)	Invitrogen	Cat# A21207	IF cells (1:500)
Sequence-based reagent	RNAscope® Probe Mm-Dpysl5-C2	Advanced Cell Diagnostics	Cat# 1112131-C2	
Sequence-based reagent	RNAscope® Probe Mm-Spast	Advanced Cell Diagnostics	Cat# 849171	
chemical compound, drug	Cholera toxin-B	List Biologicals	Cat# 103B	
chemical compound, drug	Protease inhibitors	Roche	Cat# 04693124001	
chemical compound, drug	4-20% acrylamide gels	Bio-Rad	Cat# 5671093	
chemical compound, drug	Nitrocellulose membranes	GE Healthcare Life Sciences	Cat# 10600013	
chemical compound, drug	M.O.M.® blocking reagent	Vector Laboratories	Cat# MKB-2213, RRID:AB_2336587	
Commercial assays, kits	Detergent Compatible Protein Assay	Bio-Rad	Cat# 5000116	
Commercial assays, kits	RNAscope Intro Pack for Multiplex	Advanced Cell Diagnostics	Cat# 323136	

	Fluorescent Reagent Kit v2- Mm			
software, algorithm	Image Lab Software for PC Version 6.1	Bio-Rad	RRID:SCR_014210	
software, algorithm	IQ 2 software	ANDOR Technology	N/A	
software, algorithm	Fiji/ImageJ 1.53t software	NIH	RRID:SCR_002285	
software, algorithm	Leica Application Suit X software	Leica	RRID:SCR_013673	
software, algorithm	Leica LasAF software Version 2.6.3.8173	Leica	N/A	
software, algorithm	Slidebook software Version 2022	3i	RRID:SCR_014423	
software, algorithm	IN Cell Developer Toolbox software	GE Healthcare	N/A	
software, algorithm	Cell B software	Olympus	N/A	
software, algorithm	Adobe Photoshop	Adobe	RRID:SCR_014199	
software, algorithm	GraphPad Prism 8	GraphPad	RRID:SCR_002798	
other	PureBlu™ DAPI Nuclear Staining Dye	Bio-Rad	Cat# 1351303	

other	Alexa Fluor 568-streptavidin	Invitrogen	Cat# S11226 RRID:AB_2315774	IF tissue (1:1000)
other	Opal Dye 520	Akoya	Cat# FP1487001KT	IF tissue (1:750)
other	Opal Dye 620	Akoya	Cat# FP1495001KT	IF tissue (1:750)
other	Glass-bottom 4-well chambered coverslips	Ibidi	Cat# 80427	
other	Glass-bottom 35 mm imaging dish	Ibidi	Cat# 81158	
other	Micro-feather ophthalmic scalpel	Delta Microscopes	Cat# 72045-45	
other	Fuji Medical X-Ray Film	Fujifilm	Cat# 16195209	
other	Molecular Imager GS800	Bio-Rad	Cat #170-7980	
other	ChemiDoc Imaging System	Bio-Rad	Cat# 12003153	